Review Article

Work Function: Fundamentals, Measurement, Calculation, Engineering, and Applications

Lin Lin,[1] Ryan Jacobs,[1] Tianyu Ma,[1] Dongzheng Chen,[1] John Booske,[2,*] and Dane Morgan[1,†]

[1] *Department of Materials Science and Engineering, University of Wisconsin-Madison, USA*

[2] *Department of Electrical and Computer Engineering, University of Wisconsin-Madison, USA*

(Received 26 February 2022; revised 5 November 2022; accepted 18 January 2023; published 22 March 2023)

The work function, which is the energy barrier for an electron escaping from the surface of a material, is a fundamental material surface property with many applications spanning energy harvesting, heterogeneous catalysis, vacuum electronics, and solid-state electronics. In this review, we define different aspects of the work function through an electrostatic potential treatment. We discuss in detail the role of electric fields, especially the heterogeneous surface patch field, in order to clarify potential points of confusion about work-function measurement and interpretation. We review standard experimental approaches to measure work function and the use of density-functional theory as a computational tool to predict work function. We then discuss the influence of materials chemistry and structure on work-function trends. We also discuss the role of work function in various applications, including a particular focus on relative electron energy-level alignment. Finally, we discuss two common approaches for engineering work-function values for specific applications: tuning the Fermi level and tuning the surface dipole. This review provides guidance for researchers interested in the intersection of work function, surface characterization, surface and interface physics and chemistry, and materials and device design for a wide array of technologically relevant applications.

DOI: 10.1103/PhysRevApplied.19.037001

I. BASIC PHYSICS OF THE WORK FUNCTION

The work function (represented by the symbol Φ in the remainder of this paper), generally defined as *the minimum energy required (or minimum work required) to remove an electron from the material to vacuum*, is a useful physical quantity of a material surface. However, this definition is imprecise and not unique, which has caused significant confusion about the meaning of the work function when measured with different approaches (e.g., whether the measured work function is the value of one specific surface or the average of all the surfaces). The origin of such confusion is that the energy to remove an electron from a material can depend on how it is removed, under what applied fields, and where the electron ultimately ends up in the vacuum. As a result, it is not always clear how these factors influence the results of given measurements of work function, e.g., photoelectron spectroscopy or thermionic emission. To help clarify these issues, here we carefully describe the physics controlling the energy of an electron outside a material. We then relate this energy to standard definitions of the work function and discuss how to extract the work function from a measurement.

A. Definition of the work function, influenced by electric field and surface inhomogeneity

Conventionally, the work function is simply defined as the energy difference between the vacuum level and the Fermi level [1,2] (see at the center of Fig. 1):

$$\Phi = E_{\text{vac}} - E_F. \tag{1.1}$$

As discussed here, this simple equation is often insufficient to precisely define the work function due to complexities in defining the vacuum level E_{vac}. To clarify the work-function definition, we first introduce a quantity that is closely related to the work function, denoted as $E(d)$, which is the electrostatic energy of an electron at a distance d above a (metallic) solid surface relative the Fermi level:

$$E(d) = E_{\text{vac}}(d) - E_F. \tag{1.2}$$

In Eq. (1.2), d is the magnitude of a normal vector to a specific reference surface. E_F represents the Fermi level, which is also called the electrochemical potential of the material. $E_{\text{vac}}(d)$ represents the energy level of the electron at location d that is outside of the material. Typically, this requires d to be at least a few Angstroms to have the electron no longer affected by the energetics inside the solid.

*jhbooske@wisc.edu
†ddmorgan@wisc.edu

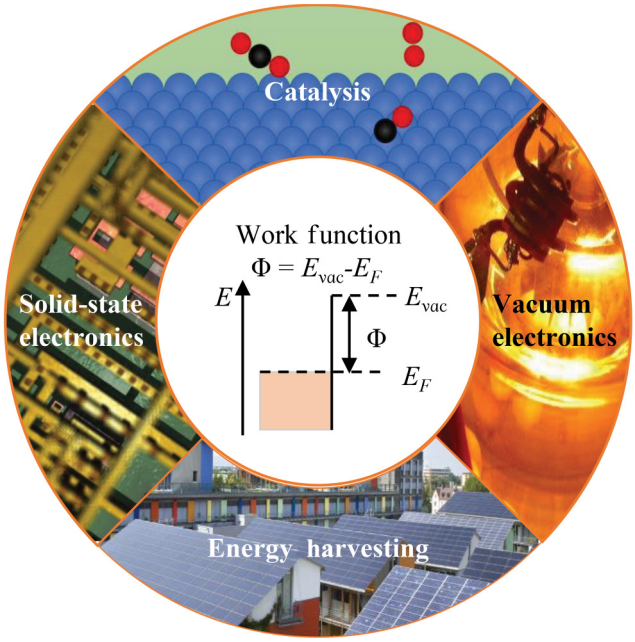

FIG. 1. Several application areas where work-function engineering is involved, including vacuum electronics, solid-state electronics, catalysis, and energy harvesting. Photo credits: Jim Pickett, David Carron, Andrew Glaser.

Therefore, $E_{vac}(d)$ is often referred by its colloquial name of vacuum (energy) level (therefore with the subscript "vac"). $E_{vac}(d)$ is rigorously defined as the rest energy of a free stationary electron outside a material at position d, given with respect to some reference. Generally, the choice of the reference energy has no impact on the work function and related quantities, as long as the same reference is also used for E_F. Since the electron has zero kinetic energy in the definition of $E_{vac}(d)$, it is equivalent to the electrostatic potential energy of the electron. $E_{vac}(d)$ is in general a function of the position vector $\mathbf{d}(x, y, d)$, where (x, y) denotes the position in the plane of the surface. In the following sections, when discussing homogeneous surfaces, we generally drop the (x, y) from the argument and just consider $E_{vac}(d)$, which is equal to $E_{vac}(\mathbf{d})$ evaluated at some fixed (x, y). On the other hand, we specify the corresponding (x, y) positions when discussing heterogeneous surfaces. Generally, $E_{vac}(d)$ is not constant with d due to the electric fields outside the material.

$E(d)$ can be used to better understand the concept of work function under different electric field conditions. To help clarify how $E(d)$ behaves versus d, and how the corresponding work function Φ is related to $E(d)$, in Secs. I A 1 through I A 3 we discuss the vacuum energy-level profiles above homogeneous and heterogeneous (also called "patchy") metal surfaces, with and without external electric fields. Figures 2–4 show the energy diagrams of these different conditions. We also include a summary of the typical values of tolerance for the quantities related to work-function physics that have been discussed here, and corresponding equations for these values (see Appendix I after the main text).

1. Homogeneous surface, no external electric field

The first and the simplest case is a homogeneous surface with one work function and zero external electric field above the surface, as shown in Fig. 2. As an electron moves out from the surface, the potential energy of the electron is initially quite complex due to still being coupled to the electronic structure of the material, but the electron then becomes a free electron after moving a few Angstroms from the surface, with the image-charge potential energy $E_{img}(d)$ being a good approximation for its $E_{vac}(d)$:

$$E_{img}(d) = -\frac{e^2}{16\pi\varepsilon_0 d}. \tag{2}$$

With such image-charge potential energy, $E(d)$ rapidly increases within the first 1 to 2 nm, and then becomes approximately constant beyond a distance of a few nanometers from the surface, as shown in Fig. 2. Since there is no significant external electric field to further influence this electrostatic potential, this constant energy level will extend to infinity. Strictly speaking, the image-charge interaction rigorously extends to infinity, but here we treat it as going to zero at about 5 nm. This cutoff distance of 5 nm is chosen for convenience and ease of calculation, as the total change in electrostatic energy from 5 nm to infinity is just 0.072 eV, which is negligible for most purposes. In this case, the work function Φ is defined as the value of $E(d)$ for $d \gtrsim 5$ nm.

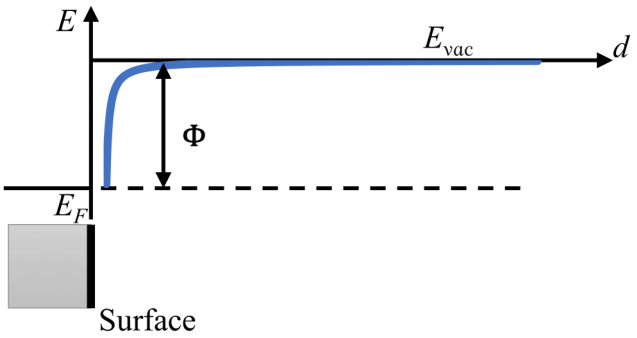

FIG. 2. The electron energy diagram above a surface with Fermi level, vacuum level, and the definition of work function for a homogeneous surface without external electric field. In this case, the vacuum level is flat after the image-charge potential stabilizes when the distance to the surface increases.

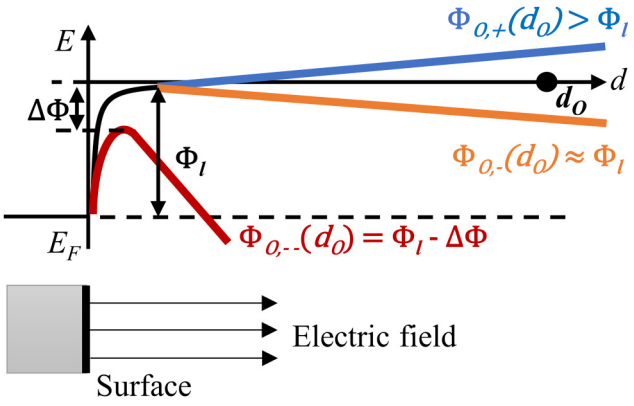

FIG. 3. The electron energy diagram above a surface with Fermi level, vacuum level, and the definition of local work function for a homogeneous surface with an external electric field. The three curves correspond to an applied field that is normal to the surface and positive (pointing away from the surface, subscript "+", blue), weak negative (pointing towards the surface, subscript "-", orange), and strong negative (subscript "- -", red).

2. Homogeneous surface, with external electric field: the observed work function

The simple case discussed in Sec. I A 1 almost never exists in real systems. There is almost always some additional electric field other than the image-charge field present in the vacuum region. Such an additional field may be induced by the charges on the nearby parts of the surface, called *patch field* (described in more detail in Sec. I A 3), or other charges in the nearby environment, called *applied field*.

In this section, we discuss the impact of the applied fields on $E(d)$ and the corresponding work functions. Such fields are sometimes applied intentionally to pull off electrons, e.g., the fields applied between the cathode and anode in electron emission, or sometimes created inadvertently, e.g., the fields that occur in ultrahigh vacuum experiments due to local work function difference between a sample and a vacuum chamber wall (also known as Volta potential). In the presence of an applied field, the vacuum energy level and $E(d)$ usually do not converge to a constant at infinity (cf. Fig. 3), and the definition of work function discussed in Sec. I A 1 is no longer valid [3].

In this situation, it is generally desirable to define the work function to be equal to $E(d)$ for point d that is close enough to a relevant surface of interest such that the external-field-induced potential change between the surface and d is small, but far enough that the image-charge potential of d is close to its value at infinity. This condition is usually met for $d \sim 5$ nm under a *weak applied field* (defined and discussed more below). Thus, we see that a natural definition for the work function in the case of weak fields is to set it equal to $E(d)$ for $d \sim 5$ nm. This definition is "the work function" discussed by most researchers, and because it requires being so close to a surface, it is fundamentally *local* in nature. We here denote this *local work function* as Φ_l and the *local point* where Φ_l is evaluated as $d_l \sim 5$ nm.

$$\Phi_l = E(d_l) = E_{\text{vac}}(d_l) - E_F. \tag{3}$$

Because the applied fields do not significantly modify the potential at this distance, the local work function under this weak-field condition is determined only by the surface itself, making the local work function an intrinsic surface property. It should be noted that the discussion of Φ_l above is based on the assumption that the applied field does little work on the electron in the first few nm above the surface, thus resulting in the *weak-field* limit. Otherwise, it is within the *strong-field* limit, where the work-function behavior is quite different (discussed more below). Further discussions and typical values for these fields are included in this section and in Appendix I.

These non-image-charge additional fields are ubiquitous as they are created by different surface terminations and many experimental setups. The homogeneous surface with weak external fields is a canonical situation, making Φ_l the most common type of work function. However, it is often more convenient or even necessary to measure the energy of the electrons much farther from the surface than the local distance, which can impact the interpretation of the measurements. To clarify this situation, we note that in the presence of a non-image-charge field, when measuring the behavior of an electron at an observation point O at a distance d_O from the surface, $E(d_O)$ might no longer be the energy needed to move that electron from inside the surface to O because of the nonflat nature of $E(d)$ under these conditions (e.g., the negative-field cases in Fig. 3). Instead, the energy to move the electron from inside the surface to point O is the maximum electrostatic energy along the lowest energy pathway from the surface to O, i.e., a barrier energy. We define this measured barrier energy as the *observed work function at O*, denoted $\Phi_O(d_O)$:

$$\Phi_O(d_O) = \max_{d \le d_O}(E(d)) = E(d_b). \tag{4}$$

Here we denote the distance from the surface to the point associated with this barrier energy as d_b. The point corresponding to this energy barrier is typically the saddle point of the $E(\boldsymbol{d})$ landscape, i.e., the minimum along the directions parallel to the surface (especially for a heterogeneous surface, see Sec. I A 3) but the maximum along the normal direction. This barrier energy, also known as the observed work function, controls many measurements, which are further introduced in Sec. II.

The observation point is often quite far from the surface (e.g., millimeters or more in many electron emission experiments) and the relationship between $\Phi_O(d_O)$ and Φ_l depends on the measurement situation, e.g., the magnitude

of any external electric fields. The relationships between $\Phi_O(d_O)$, Φ_l and the external electric field are summarized as below, where we assign the positive electric field to be pointing out from the surface:

(1) When the external field is positive (blue curve in Fig. 3), the field will create an additional barrier to prevent the emitted electrons from further leaving the surface, making $\Phi_O(d_O) > \Phi_l$.

(2) When the external field is negative but not too strong (no larger than several 10^6 V/m, see Appendix I for calculation details) (orange curve in Fig. 3), the electrostatic energy maximum will occur just after the influence of the surface image charge stops being felt, which can be considered at the local point (i.e., $d_b = d_l$). In this case, the observed work function will be equal to the electrostatic energy at the local point, which in turn is equal to the local work function. Therefore, $\Phi_O(d_O) \approx E(d_l) = \Phi_l$. Note that this will not hold if the applied field is comparable to the image-charge field at a few nm away from the surface (approximately 10^8 V/m, see Appendix for calculation details), since this will change the values of $E(d_l)$, see case (3) below.

(3) If the negative field has a strength comparable to the image-charge field within several nm from the surface (approximately 10^8 V/m) (red curve in Fig. 3), the potential curve and its maximum will be significantly bent to lower energy, leading to a decrease of $\Phi_O(d_O)$ by the amount of

$$\Delta\Phi = \sqrt{\frac{e^3 F}{4\pi\varepsilon_0}}, \tag{5}$$

where e is elementary charge and F is the external electric field. This reduction is called Schottky effect. The effect is associated with a model Schottky [4,5] applied in 1923 that failed to quantitatively explain field emission, but it is still a very useful factor in electron emission, which is further discussed in Sec. II C. In this strong negative-field limit, it is common to still refer to the observed work function $\Phi_O(d_O)$ defined in Eq. (4) as a work function, which is reasonable as $\Phi_O(d_O) = E(d_l)$ still holds. However, $\Phi_O(d_O)$ under a strong field is no longer equal to Φ_l nor any intrinsic materials surface property, but instead a function of the applied field.

3. Heterogeneous surface, without and with external electric field: the patch field

The discussion above focuses on the case of a homogeneous surface with one local work function over the entire surface. However, in many materials, obtaining a homogeneous work-function surface is extremely difficult because of the difficulty in producing and maintaining a large homogeneous single-crystal surface with only one orientation and termination. Most materials will consist of multiple grains with different surface orientations and terminations, and thus contain different local work functions. Some may also have heterogeneous surface-dipole coatings that modify the local work functions in a patchy manner. The presence of multiple different local work functions on one material surface will introduce further complexity into the vacuum level profile and the work-function interpretation through the patch-field effect, as described below.

Figure 4(a) shows the electric field above a surface containing two surface components with different local work-function values Φ_L and Φ_H ($\Phi_L < \Phi_H$), resulting from, for example, partial coverage by a surface-dipole layer. We assume the patches are large enough that each can have a well-defined local work function following the definition given in Secs. I A 1 and I A 2, and that there are no applied fields. Since the two regions are in electrical contact and in equilibrium, the Fermi levels of the two regions are equal, and the difference in the local work functions translates to a difference in the local vacuum levels, which equates to an electrostatic potential energy difference between points just above the two surface patches. Such lateral electrostatic potential energy difference will naturally create a nonzero electric field above the surface to modify $E(d)$ even if the applied field is zero. This modification of the electrostatic energies by electric fields due to heterogeneous local work functions on one surface is often called the patch field effect, first discussed in the 1930s [6].

Figures 4(a) and 4(b) illustrate how the patch fields transform $E(d)$ above different patches. Just above each patch but far away from the patch edges, the $E(d)$ will look similar to that of the corresponding homogeneous surface, as shown in Fig. 4(b). As the electron moves farther above the two patches, the difference in $E(d)$ above these patches decreases until $E(d)$ above both kinds of patches merges into a single value. This convergence is required by the fact that for an electron far enough from the material, the local field effects must drop to zero and the electrostatic energy must converge to a single value, which is the area-weighted average value of the two local work functions across the surface: $\Phi = \eta\Phi_L + (1-\eta)\Phi_H$, where η is the coverage fraction of Φ_L. Therefore, when moving away from the surface, the electrostatic potential energies (vacuum levels) above the Φ_L and Φ_H patches will increase and decrease, respectively.

In this two-patch situation there are two well-defined local work functions, Φ_L and Φ_H. However, many measurements do not directly measure either local work function. Without the presence of applied fields, if the measurement point O is relatively far away from the surface, the observed work function $\Phi_O(d_O)$, is set by the asymptotic value of the electrostatic energy, which is the area-weighted-average work function Φ.

If there is a negative applied electric field, $E(d)$ will have a term that decreases with distance from the surface.

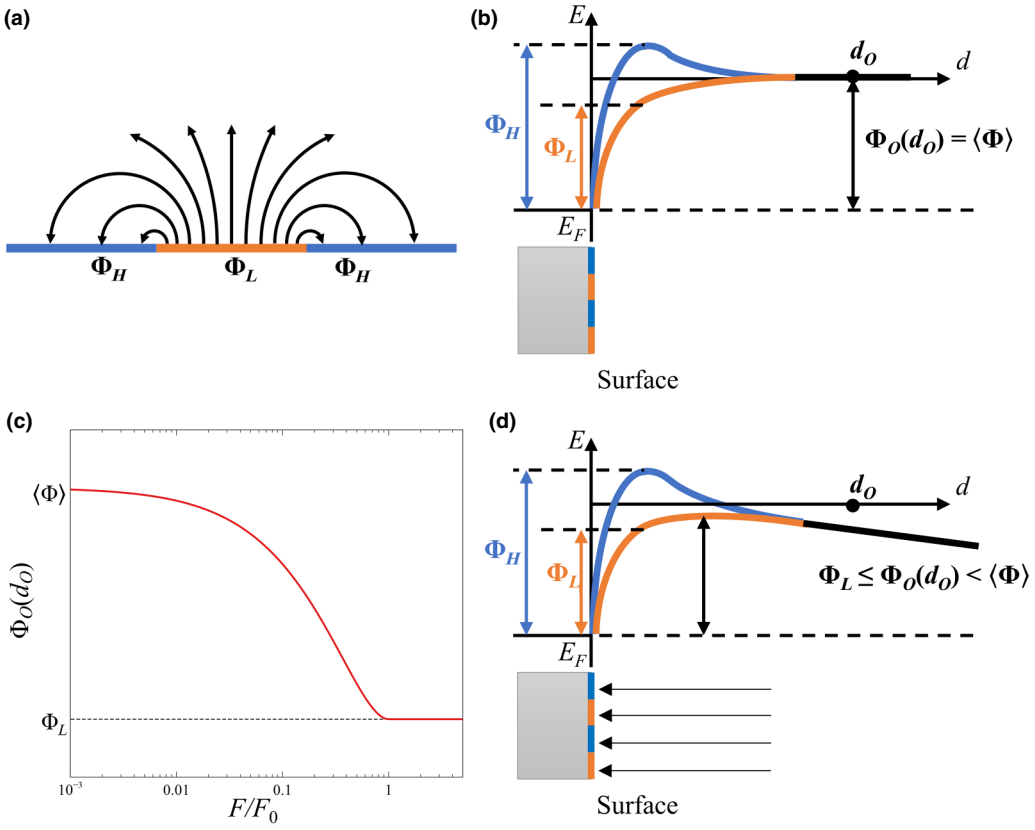

FIG. 4. (a) Schematic of the patch electric field distribution (in the absence of an external field) above a lower local work function (Φ_L) patch bordered by higher local work function (Φ_H) areas. The induced lateral surface dipole field draws electrons emitted from the Φ_L patch back toward the Φ_H surfaces. (b) The energy diagram without an applied field above a patchy surface, with the observed work function at point O, $\Phi_O(d_O)$, equal to the average work function on the surface. (c) Observed work function versus applied electric field plot derived from Eq. (5.1), showing $\Phi_O(d_O)$ decreases as external field increases, until Φ_L when the field reaches F_0. (d) The energy diagram with a negative external field above a patchy surface, suggesting $\Phi_O(d_O)$ becomes lower.

This term will generally reduce the observed work function $\Phi_O(d_O)$ from Φ towards a lower value above Φ_L patches because of the lower local work-function value [as shown in Figs. 4(c) and 4(d)]. The exact value of $\Phi_O(d_O)$ depends on the field strength, the patch size, and the local work-function difference. Bundaleski *et al.* computationally determined the quantitative effect of this patch field by showing the expression of $\Phi_O(d_O)$ for a surface consisting of patches with two work-function values Φ_H and Φ_L [7,8] can be written as

$$\Phi_O(d_O) = \Phi - (\Phi - \Phi_L)\frac{F}{F_0}\left(1 + \ln\frac{F_0}{F}\right), \qquad (6.1)$$

with

$$F_0 = \frac{\Phi_H - \Phi_L}{ek\sqrt{S}}, \qquad (6.2)$$

where k is a constant depending on the exact patch geometry that is typically close to 0.5 when the patch shapes are not very elongated (for example, close to circular or square shapes), S is the area of a single patch (assumed to be the same for each type of patch), and F is the applied field. Equation (6.1) predicts that $\Phi_O(d_O)$ decreases as the applied field increases, ultimately reaching Φ_L when F reaches F_0. F_0 can therefore be understood as the critical field needed to reveal the lowest local work function by negating the patch-field effect. Neglecting prefactors on the order of magnitude of 1, the value of F_0 can be roughly estimated through dividing the surface work-function difference (in volts) by the patch lateral size dimension. We note here that typically F_0 is still too weak to trigger significant Schottky effect discussed in Sec. I A 2. It should be noted that to have physical meaning, Eq. (6.1) is only valid for the case when $F \leq F_0$. In the case of $F > F_0$, $\Phi_O(d_O)$ will always approximately equal Φ_L until the Schottky effect is large enough to significantly lower $\Phi_O(d_O)$. In other words, when $F > F_0$, the applied external electric field is strong enough to overwhelm the patch fields arising from local work-function heterogeneity, and electrons collected at remote location O are observed to arrive consistent with having escaped an energy barrier of the lowest

local work function, Φ_L. *An important implication of this result is that* $\Phi_O(d_O)$ *on patchy surfaces is not necessarily equal to any local work function of any surface and must be interpreted with great care.* Further discussion of the impact of patch-field effects on experimental work-function measurements is included in Secs. II A 2 and II C.

The discussions in Secs. I A 2 and I A 3 illustrate that there are at least two common work-function definitions. The first is the local work function, which is an intrinsic property of the corresponding material surface. The second is the observed work function, which is controlled by the field-modified energy to remove the electron and may or may not be equal to any local work function of a specific surface, depending on patch- and applied-field conditions. Going forward in this review, unless otherwise specified, the term *work function* refers to the *local work function of a surface* when discussing work-function calculation, application, and tuning mechanisms. We also make frequent use of the observed work function since it is the quantity directly available through work-function measurement, which is further discussed in Sec. II.

4. Work function and related concepts in semiconductors

The Fermi level in a semiconductor can have a range of values, typically from just below the valence-band maximum (VBM) (in the limit of degenerate p-type doping) to just above the conduction-band minimum (CBM) (in the limit of degenerate n-type doping). For example, for an undefected ideal semiconductor at a temperature just above absolute zero, the Fermi level resides in the center of the band gap, where the density of states is zero. In the limit of the semiconductor being n type (p type), the Fermi level resides at the CBM (VBM), and the work function is equal to the electron affinity (ionization energy). The ionization energy (IE) is the energy required to remove an electron from the VBM to the local vacuum level and the electron affinity (EA) is the energy gained by adding an electron from the local vacuum level to the CBM, as shown in Fig. 5(a). The ionization energy, electron affinity, and work function are all surface electronic properties of a material, as shown in Fig. 5 [1,2]. For the case of a degenerately doped semiconductor, the Fermi level may be sufficiently n type (p type) such that the work function has a lower (higher) energy than the electron affinity (ionization energy). In the nondegenerate doping case, direct knowledge of the work function and band gap provide values of the resulting ionization energy and electron affinity. Moreover, the work function plays a significant role in interface chemistry and electronic device design because it dictates the band alignment between materials in electrical contact [2,11,12]

Compared to metallic systems, semiconductors typically have much lower free carrier densities and thus much longer screening lengths. Consequently, the influences of ambient electric fields and surface states result in near-surface band bending, making ionization energy, electron affinity, and work-function physics more complex. Historically, the influence of patch field on the interpretation of ionization energy and electron affinity has seldom been investigated by researchers. The (typically) much lower free carrier density in a semiconductor versus a metal results in a thicker interfacial charge accumulation region, which may influence the vacuum level landscape and induced patch-field shape. Nevertheless, since the basic physics of electrostatics in the vacuum are the same for different surfaces, it is expected that ionization energy and electron affinity exhibit similar behavior with respect to local and nonlocal vacuum levels as well as patch and applied fields as the metal work function [2,13].

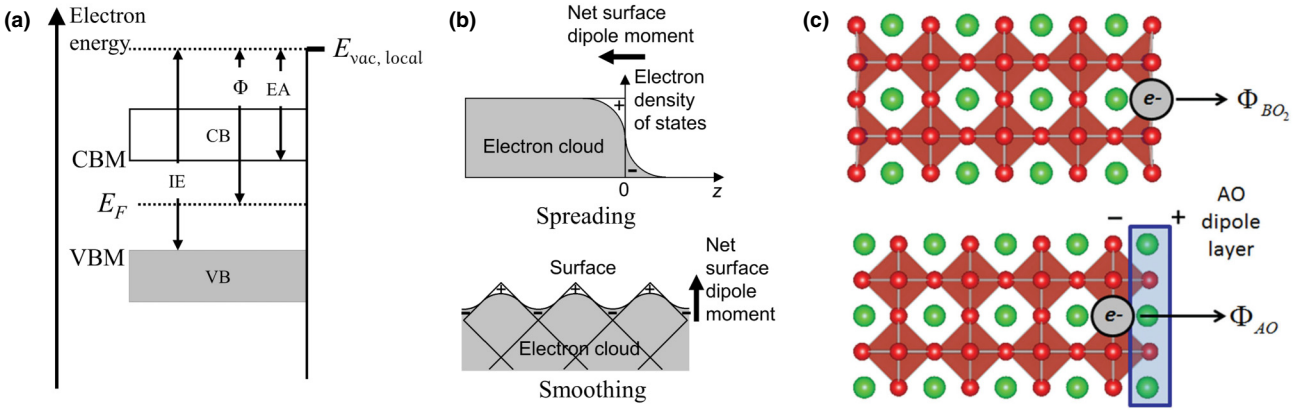

FIG. 5. (a) Schematic band diagram and work function for a (nondegenerate) semiconductor together with its ionization energy (IE) and electron affinity (EA) inspired by Fig. 1 of Ref. [2]. (b) The spreading and smoothing effect of electron clouds, creating dipole moments on a simple metal suggested by Smoluchowski in Ref. [9]. (c) The atomic structure of a perovskite, an example of polar materials where the AO- and BO_2-terminated surfaces have opposite surface atomic arrangements and therefore opposite dipoles. (From Ref. [10] ©2016 WILEY-VCH Verlag GmbH & Co. KGaA, Weinheim).

B. Factors controlling the work function

The local work function of a surface can be decomposed into two parts: an intrinsic component, which depends on the energy of the electron in the material as determined by the band structure, and a surface component determined by the image-charge potential and local surface-dipole effects. To discuss the factors controlling the local work function, here we assume a well-defined local work function that is an intrinsic surface property (i.e., it is not influenced by the additional fields). The work done on the electron by the surface is determined by many multipoles, but it is generally assumed that the dipole dominates the energetics. This assumption is justified at least in part by the rapid decay of multipole fields (approximately $1/x^3$ for dipoles versus approximately $1/x^5$ for quadrupoles and even faster for higher-order multipoles) and the natural tendency for charged atoms and their compensating charge to be close together in dipole-type structures. We further assume the image-charge potential is similar among different materials, which is strictly true only for metals, but is also generally a good approximation for materials with a relatively large dielectric constant ε (e.g., ε is larger than approximately 2), since the image-charge potential energy for an electron above a dielectric is

$$E_{\text{img}}(\varepsilon) = \frac{\varepsilon - 1}{\varepsilon + 1} E_{\text{img}}(\text{metal}). \tag{7}$$

Under these conditions and approximations, the values of material work functions are determined by the material-specific electronic band structures and surface-specific surface dipoles. Given this, understanding and controlling the work function in a material is typically accomplished by modifying the bulk electronic structure, which governs the Fermi-level location relative to what we call the *intrinsic vacuum level* (the hypothetic vacuum level in the zero-surface-dipole scenario), and the surface dipole, which modifies the local vacuum level energy and makes the work function a surface-sensitive quantity.

The bulk electronic structure, determined by composition, structure, dopants, defects, pressure, and many other factors, sets the Fermi level with respect to the intrinsic vacuum level, and consequently affects the work function: a higher (lower) Fermi level results in a lower (higher) work function, assuming the surface dipole remains unchanged.

Besides the bulk electronic structure, surface properties also significantly influence the work function. As mentioned above, this modification manifests as an effective surface-dipole effect, although the detailed surface physics might be very complex. Below are some widely observed and discussed surface-dipole effects:

(1) Smoluchowski (1941) [9] showed that for a simple elemental metal, a surface dipole originates from the electron cloud on the surface seeking the lowest energy configuration, accomplished through spreading and smoothing of the electron cloud [see Fig. 5(b)]. The electron-cloud spreading creates a negative dipole and increases the work function, while the smoothing of the electron cloud has the opposite effect. The magnitudes of these two effects are typically similar in absolute value, approximately a few tenths of eV, but do not completely cancel, thus resulting in a net dipole for every surface.

(2) For a more complex material system, such as an oxide or other multicomponent system, the dipole could come from the polarity introduced by the top-most atomic layer and the layer immediately beneath it. Such dipoles can be quite large, where the energy modification could be on the scale of a few eV [10,14]. Furthermore, any changes in the surface atomic configuration, such as differences in surface orientation [e.g., (001) versus (111) surface of W] or termination [e.g., (001) SrO terminated $SrTiO_3$ versus (001) TiO_2 terminated $SrTiO_3$], surface reconstructions, or adsorbed molecules or atoms, can lead to significant changes in the charge distribution at the surface, leading to significant changes in the work function. One example is shown in Fig. 5(c).

The above discussion separately discusses the impact of bulk electronic structure and surface dipole on the work function. We note here that it is common practice to assume these two quantities act independently of each other. However, it is possible for the bulk electronic structure to alter the surface dipole and vice versa. As an example of the bulk electronic structure altering the surface dipole, an increasing Fermi level with bulk doping might fill surface states and thereby change the surface dipole. Surface changes can also effectively alter electronic structure far into the bulk of the material when the electrical screening of the material is low due to insufficient mobile charges available for screening. For example, surface adsorbates may dope electrons (holes) into the system, creating a positively (negatively) charged surface adsorbate, which acts to increase (decrease) the surface dipole, and also simultaneously raise (lower) the Fermi level of the near-surface material. Thus, for materials with low electrical conductivity (e.g., semiconductors or nontransition metal oxides), the effects of surface dipoles and bulk electronic structure modification may become coupled in the near-surface region, complicating the understanding and analysis of the work function.

II. METHODS TO MEASURE THE WORK FUNCTION

The relevance of the work function for many materials applications (see Sec. IV) makes accurate measurement and prediction crucial to both understanding material properties and materials design. Over the last century a number

of techniques have been developed to measure work functions. The most commonly used measurement methods are based on electron emission (with photo, thermionic, or field emission) and contact potential difference [1–3,11]. These methods have been previously reviewed and compared [15,16]. In this section, we discuss these methods specifically in the context of the electrostatic energy profile discussed in Sec. I. We emphasize here that, regardless of the method employed, the measured quantity is always the *observed work function* Φ_O seen at the detection probe, such as a photoelectron spectrometer, an adsorbed Xe atom, a microscopy measurement tip, or an emission-testing anode. Thus, the measured quantity is always influenced by the previously discussed effects of surface patch fields and applied electric fields so that the measured value, Φ_O, may not be equal to a local surface work function Φ_l.

A. Photoemission-based measurements

Photoemission-based measurement, typically ultraviolet photoelectron spectroscopy (UPS), is the most widely employed approach for reliably measuring the work function due to its standardized experimental setup, good electron energy resolution, and the availability of high-brightness photon sources [17]. However, we note here that one should take extra caution when processing UPS data with regard to applying a suitable bias, setting up the correct sample-detector geometric configuration, and interpreting data properly to understand how the observed work function relates to the local work function(s).

UPS directly employs the photoelectric effect by measuring the kinetic energy of a photoelectron emitted by the absorption of an incident photon. However, due to conservation of the photoelectron energy when traveling in the nonuniform vacuum level towards the electron detector, the UPS work function could not be directly derived by subtracting the photoelectron kinetic energy from the incident photon energy [3]. Consequently, as pointed out by Cahen and Kahn, the standard approach to calculate the work function from UPS data is to subtract the photoelectron spectrum bandwidth W between the Fermi edge E_F and the secondary electron cutoff $E_{\text{vac}} - h\upsilon$, from the photon energy [3] [a schematic illustration and an example are shown in Figs. 6(a) and 6(b) [3,18]].

$$\Phi_{\text{O}} = E_{\text{vac}} - E_F = h\upsilon + E_{\text{vac}} - h\upsilon - E_F = h\upsilon - W. \tag{8}$$

During a UPS work-function measurement, typically a small negative sample bias (5 to 10 V) is applied to guarantee an overall negative electric field that accelerates the photoelectrons away from the sample and towards the detector [3,19,21]. As discussed in Sec. I A, when measuring a homogeneous metal surface, this weak negative field will make the observed work function Φ_O equal to the surface local work function Φ_l. Meanwhile, as pointed out by Helander *et al*., the sample surface needs to be perpendicular to the spectrometer, in order to avoid measurement artifacts caused by geometric configuration [21]. Additionally, surface charge can significantly perturb the measured work function, so the sample must have high electrical conductivity and good electrical contact with the sample holder. If the sample is a semiconductor with poor electrical conductivity, the measurement is typically conducted on a thin-film sample [22,23], and one must carefully calibrate the Fermi edge location, commonly towards a noble metal electrode that is electrically connected to the sample surface [24].

For a heterogeneous surface, the work-function interpretation will be more complex. We emphasize our discussion in Sec. I A 3 that the patch field above a low-work-function area will decelerate electrons emitted from this low-work-function patch. Therefore, the observed work function measured by the spectrometer depends on the intensity of the applied negative electric field compared to the critical field in Eq. (6.2). In the absence of a strong applied electric field comparable to or greater than the critical field, the measured work-function value for a heterogenous surface with multiple work functions will be *a patch-area-weighted average*. As the negative applied field becomes stronger, the measured work function will decrease, asymptotically converging to *the lowest local work function* across the surface when the external field exceeds the critical field [4]. An approximate solution of Eq. (6.2) for the typical applied bias (approximately 10 V) and sample-to-detector distance (approximately 1 mm) within UPS measurement shows that one would not be able to get the lowest work function if the patch size is smaller than approximately 100 μm, assuming the work-function heterogeneity is on the order of 1 eV among different patches. This straightforward application of patch-field theory implies that nearly all cases of work-function measurement by UPS are in fact the area-weighted average of the individual patch local work functions.

Several recent experimental investigations confirm the conclusion that UPS-measured work functions are the area-weighted average of individual (patch) local work functions for microscopic patches and weak fields. Bundaleski *et al*. [8], and Schultz *et al.* [19,25] have studied the photoemission-observed work function of several example surfaces with heterogeneous work-function distributions. The results show excellent agreement with patch-field theory by observing a surface-averaged work-function value for a weak applied field, and the lowest local work-function value for a strong applied field (in comparison to the critical field). Note that it is the electrostatic potential spatial distribution—including the patch field—that causes this averaging effect, rather than the limited spatial resolution or the spot size of the photon source. That said, even if one were to illuminate a single, micron-sized,

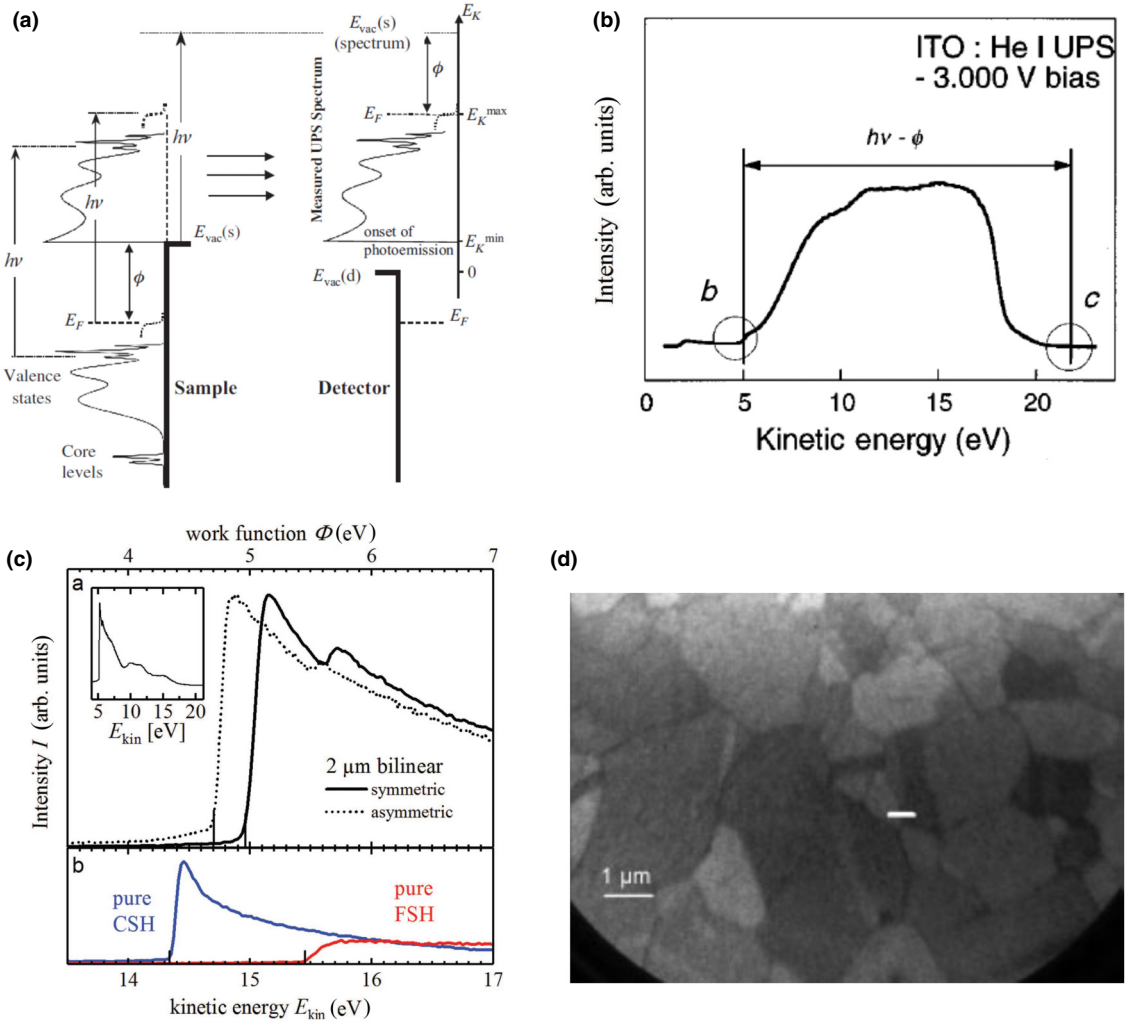

FIG. 6. (a) Schematic energy and spectroscopy diagram illustrating the procedure of subtracting work function from UPS, directly indicating Eq. (7) (from Ref. [3] ©2003 WILEY-VCH Verlag GmbH & Co. KGaA, Weinheim). (b) A set of real data for UPS-measured ITO work function (reprinted from Ref. [18] with the permission of AIP Publishing). (c) Measured work function with UPS on a heterogeneous surface with zebra-crossing coatings of CSH and FSH polymers (with 4.3 and 5.4 eV local work functions, respectively) under weak field, resulting in average measured values across the surface (from Ref. [19] ©2017 WILEY-VCH Verlag GmbH & Co. KGaA, Weinheim). The "symmetric" and "asymmetric" labels represent the measured spectrums from a 50%:50% coated surface and a non-50%:50% coated one, indicating the measurements reveal area-weighted average work-function values. (d) An example of PEEM image on polycrystalline copper (from Ref. [20] ©2006 John Wiley & Sons, Ltd.), with different work functions indicated by brightness differences. This suggests the local work functions for microscopic grains are resolvable under high applied field.

low-local-work-function grain with a highly focused photon source, the UPS measured work function would still be the area-weighted average value across a large area (e.g., millimeters in size), as long as the applied electric field is much weaker than the critical field. On the other hand, a measurement with a centimeter-sized photon spot would be able to capture the lowest local work function on a micron-sized patch if the applied field is strong enough compared to the critical field.

The discussion above excludes the influence of surface morphology on the observed work-function values. According to some studies, surface roughness may significantly modify the work function. However, different studies provide different conclusions on how the work function is modified. Some argue that the work function decreases, due to local-field enhancement introduced by surface roughness [26], while others suggest either a work-function increase [27] or a decrease [28,29] with increased surface roughness. Overall, there does not appear to be a consistent understanding of the physical mechanism behind morphological influences on the work function at this time [30–34]. Further work is still needed to reveal the relationship between the observed work function, surface morphological features such as roughness, and the impact on observed work function. Nonetheless, tuning surface morphology to include extremely high-aspect-ratio

features has been widely used in field emission to reach a high local field. For example, typical field emitters have a sharp-tip shape, which provides a huge local field enhancement that lowers the work function by the Schottky effect as well as enabling Fowler-Nordheim tunneling for field emission (see Secs. II C and IV A).

To measure the lowest local work function on a heterogeneous surface from a remote point, a sufficiently large field is required in order to overcome the patch-field effect. Such fields are possibly present in the case of photoemission electron microscopy (PEEM) [20,35–38], with an approximately 1 V/μm typical applied field that is capable of canceling out the patch-field effect on a surface with $>\sim 1$ μm patches and <1 eV work-function differences. As a result, the work-function distribution across the sample surface is expected to be resolvable, and it is possible to map out the lateral work-function distribution. An example of such a mapping is given in Fig. 6(c), where the local work-function difference indicated by different brightness areas (brighter regions indicate lower work functions). In order to obtain the absolute work-function values, a spectroscopic measurement is also needed during PEEM experiments [20].

Wandelt *et al*. proposed alternative approaches to obtain the local work-function value [39]. These approaches include photoelectron spectroscopy of adsorbed xenon (PAX) and two-photon photoelectron spectroscopy (2PPES). PAX uses the $5p$ core level energy shift of adsorbed xenon atoms to monitor the surface local electrostatic potential, while 2PPES measures the energy levels of hydrogenlike surface states that transiently trap photoelectrons [39]. In both cases, the local electrostatic potential energies (vacuum levels) on the surface have been directly measured, which will yield surface local work-function values.

Besides using photoelectron spectroscopy, which measures the secondary electron cutoff of the photoelectron spectrum, the photoemission work function can also be extracted by measuring the photoemission current. This current corresponds to the quantum efficiency (i.e., the ability of an incident photon beam to liberate electrons), which is proportional to $(h\nu - \Phi)^2$ [40]. Therefore, the work function can be extracted by fitting the square root of photoemission current versus the photon energy and finding the intersection with the horizontal axis [41,42]. Again, this method should comply with all of the arguments on applied voltage and patch-field effect provided above.

B. Measurement based on contact potential difference (Kelvin probe)

The work function can also be obtained by measuring the contact potential difference (CPD). The CPD is the electrostatic potential difference between surfaces of two metals that are in electrical contact, therefore it is equal to the local work-function difference between two surfaces with the proper experimental setup containing a well-characterized reference metal surface. This method is known as Kelvin probing (KP). Modern KP experiments are frequently performed with an atomic force microscope (AFM) using a noncontact operation mode setup, called Kelvin probe force microscopy (KPFM) [43–46]. The probe (cantilever and tip for the case of KPFM) is usually made of a conductive material with a well-known local work-function value and high chemical stability, e.g., tungsten, gold, platinum, or silicon coated with such metals.

The general process of KPFM experiment is indicated in Fig. 7(a) [46]. In a typical KP and KPFM experiment, the sample and the tip are in electrical contact through an external circuit, and an ac voltage is superimposed onto a dc bias applied between the sample and the probe. The external electrical circuit connection ensures that the sample and probe tip share a common Fermi level. The total voltage between the tip and the sample is

$$V = (V_{\mathrm{dc}} - V_{\mathrm{CPD}}) + V_{\mathrm{ac}} \sin \omega t, \tag{9.1}$$

where V_{CPD} is the contact potential difference and ω is the frequency of the ac voltage. The force between the sample and the tip can be derived as

$$\begin{aligned} F &= \frac{1}{2}\frac{dC}{dz}V^2 \\ &= \frac{dC}{dz}\left[\frac{1}{2}(V_{\mathrm{dc}} - V_{\mathrm{CPD}})^2 + \frac{1}{4}V_{\mathrm{ac}}^2 \right. \\ &\quad \left. + (V_{\mathrm{dc}} - V_{\mathrm{CPD}})V_{\mathrm{ac}} \sin \omega t - \frac{1}{4}V_{\mathrm{ac}}^2 \cos 2\omega t\right], \end{aligned} \tag{9.2}$$

where C is the capacitance between the sample surface and probe. This force has three frequency components, corresponding to 0, ω, and 2ω, and the ω component is proportional to $(V_{\mathrm{dc}} - V_{\mathrm{CPD}})$. Therefore, when tuning the dc voltage bias to make the ω force component zero (or as small of an absolute value as possible in a real experiment) the applied V_{dc} will be equal to V_{CPD}, which is also equal to the work-function difference between the sample and the probe [43]:

$$\Delta\Phi = eV_{\mathrm{CPD}} = eV_{\mathrm{dc}}. \tag{9.3}$$

Kelvin probing directly measures the force derived from the electrostatic potential gradient influence on the probe. In the electrostatic potential profile landscape, V_{dc} compensates the electrostatic potential difference between the sample and the probe. Therefore, $\Delta\Phi$ in Eq. (9.3) can be considered as the difference between the sample's observed work function at the probe $\Phi_{\mathrm{O}}(\mathrm{probe})$, and the probe tip (local) work function. In a macroscopic (large-area tip) KP experiment, $\Phi_{\mathrm{O}}(\mathrm{probe})$ might be equal to the

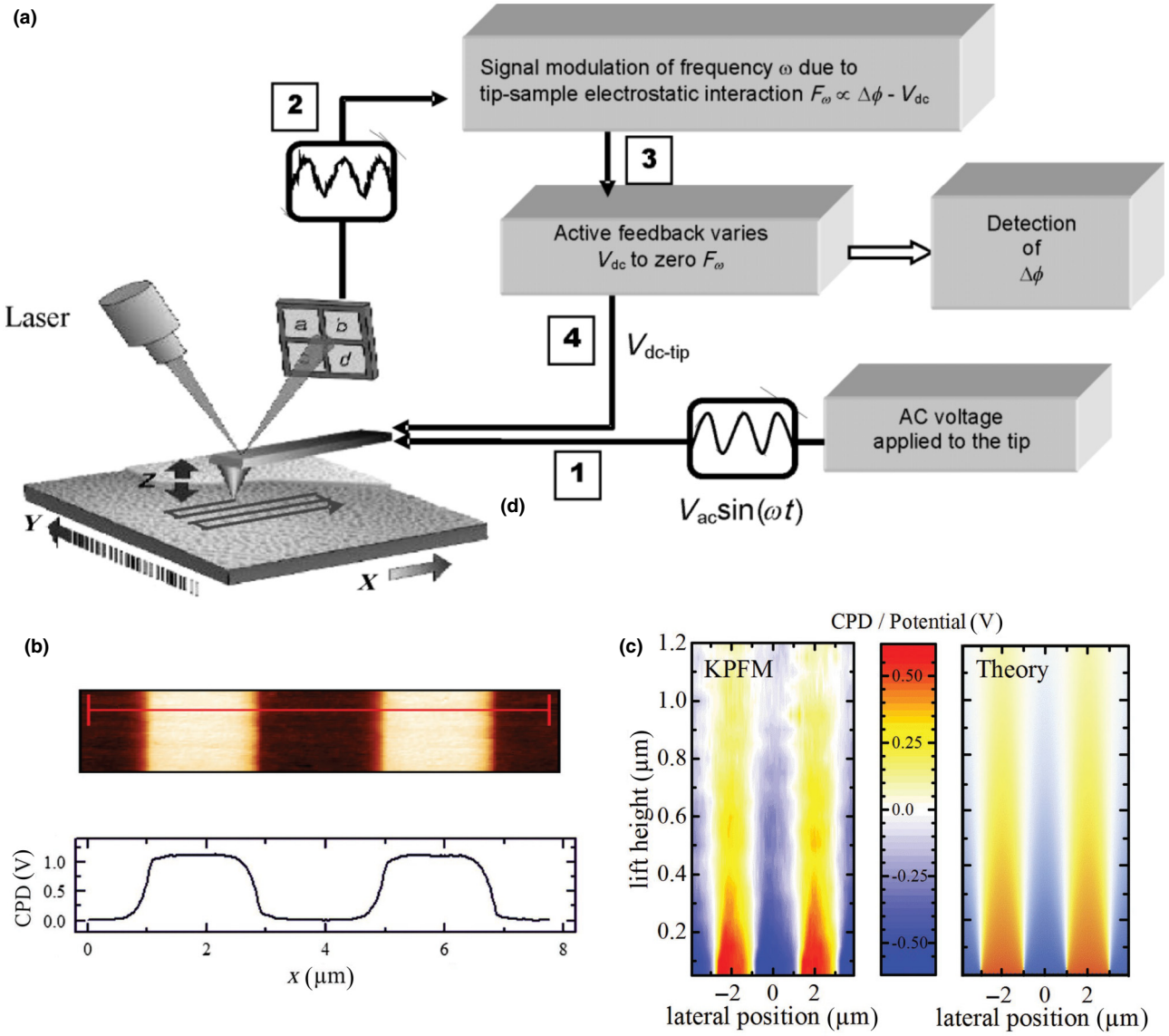

FIG. 7. (a) Schematic diagram of KPFM setup for work function measurement (from Ref. [46] ©2006 WILEY-VCH Verlag GmbH & Co. KGaA, Weinheim). (b) An example of KPFM work-function mapping for a heterogeneous surface (from Ref. [19] ©2017 WILEY-VCH Verlag GmbH & Co. KGaA, Weinheim). The zebra-crossing pattern deposited with two different organic molecules, namely FSH and CSH, have a local work-function difference of 1.1 eV, which is directly detectable via KPFM. (c) An example of PEEM image on polycrystalline copper (from Ref. [19] ©2017 WILEY-VCH Verlag GmbH & Co. KGaA, Weinheim), with different work functions indicated by brightness differences. This suggests the local work functions for microscopic grains are resolvable under high applied field.

average work function on the sample surface. In contrast, the small distance between the tip and sample (approximately 10 nm) in a typical KPFM experiment means that the observation point is the local point, enabling the direct measurement of the sample's local work function, unperturbed by patch-field averaging. Moreover, since KPFM is a microscopic technique, it is also possible to map out the lateral distribution of the surface local work function and simultaneously provide a lateral spatial measurement resolution on the order of the probe tip size. As a result, KPFM measurements can provide local, rather than the average, work-function values across the surface [see Fig. 7(b)] [19]. Additionally, if placing the KPFM probe tip at a position that is farther away from the surface, it could measure the electrostatic potential of the corresponding position, which enables direct mapping of the potential landscape of a patch field, with a nice example shown in Fig. 7(c) [19].

Many KP and KPFM instruments are operated in an atmospheric ambient environment, so the surface may

experience contamination (e.g., adsorption of O_2, H_2O, CO_2) that will influence the work function. For example, Kim *et al*. have reported that KPFM measured work functions of indium tin oxide (ITO) in air or Ar disagree with UPS measured work functions measured under ultrahigh vacuum (UHV) conditions [22]. However, this is a consequence of the surface contamination, and not because the KP and KPFM work-function measurement is fundamentally unreliable. As Beerbom *et al*. pointed out, UHV-based KP provides highly reliable work-function measurements [23]. Another advantage of KP and KPFM is its nonperturbative nature due to its noncontact measurement mode, avoiding irreversible damage on the surface. Surface damage can potentially be an issue with high-energy photons in photoemission-based methods. Beerbom *et al*. found the work function of ITO decreased from 4.55 to 3.90 eV after the UPS measurement, and this decrease is an irreversible change related to surface chemistry, suggesting the surface dipole is permanently altered by the ultraviolet beam. Consequently, the KPFM work function would be expected to offer greater validity and reliability in this particular use case [23].

C. Other experimental methods—thermionic emission and field emission

There are additional approaches to measure the work function by exploiting other mechanisms for electron emission from the surface. These include thermionic emission, where the electron gains enough thermal energy to leave the surface at high temperature, and field emission, where the electron tunnels through a narrow energy barrier resulting from a strong external electric field.

The Richardson-Laue-Dushman (RLD) equation [24,47] with Schottky barrier lowering [4,5] [Eq. (5) mentioned in Sec. I A 2] describes the behavior of thermionic emission current density J_T at temperature T from a cathode with a single work function (i.e., no patch field), when electron emission is temperature limited (TL), as opposed to space-charge limited,

$$J_T = AT^2 \exp\left(-\frac{\Phi}{kT}\right). \tag{10}$$

The temperature variation method, also called the "total current" method, is a frequently used method to measure the work-function value. In this method, the value of the work function Φ is found by fitting the RLD equation to experimental data [48–50]. In particular, the standard practice is to fit a straight line to a graph of $\ln(J_T/T^2)$ versus $1/T$, extracting an *apparent* work function from the slope. However, it is important to recognize that this apparent work-function value is also associated with an apparent value for the pre-exponential Richardson constant A.

When calculating the theoretical value of A, the electrons are assumed to act as a noninteracting electron gas, where the energy levels of the electrons are determined using the Fermi-Dirac (FD) distribution. The value of A is obtained by calculating the rate of which electrons will overcome an energy barrier equal to the work function from thermal excitations. This approach gives a value of $A_0 = 4\pi mek^2/h^3 \approx 120\ \mathrm{A/cm^2/K^2}$ [40]. However, this value ignores a number of factors, including the fact that real materials have very different densities of states than a noninteracting electron gas, electrons will reflect due to quantum mechanical scattering at the surface (or, more precisely, the rates of tunneling from surface to vacuum states may be quite different from the simple assumptions of the traditional derivation [51]), and potentially other factors (e.g., electron depletion during emission [40,52,53]). In general, these effects all tend to lower the actual value of A below A_0, consistent with what is typically found experimentally and the requirement of detailed balance between metal and electron vapor [54]. A fully quantum mechanical treatment of A was performed by Voss *et al*. [51], resulting in predicted values of A for W (110) coated with Cs in reasonable agreement with experiments that range from approximately 40 to 200 times smaller than A_0.

Meanwhile, examination of a number of published thermionic emission articles reveals that there are many cases in which the current-versus-temperature data deviate, sometimes significantly, from the RLD equation. This is an incentive for additional research producing more physically complex emission models. It has been suggested that the dimensionality of the emitter could cause the emission current density to deviate from the RLD equation. Ang *et al*. have studied the thermionic emission current density through a graphene-based Schottky interface, suggesting a pre-exponential term proportional to T^3 rather than T^2. More generally, a T^β dependence is likely to be present, originating from the dimensionality and nonparabolic band structure [55–57]. Furthermore, the emission model suggested by Chen *et al*. [4] shows that current emitted from a heterogeneous cathode surface can deviate significantly from the simplified RLD equation, which can be accurately predicted by a more complex model incorporating patch fields, Schottky effect, and space-charge physics. Recent additional studies in our group suggest that for a heterogeneous cathode surface with multiple local work-function values, when simultaneously fitting both A and Φ, patch-field-caused distortions from Eq. (10) to the J versus T curve can result in the fitted work-function value being artificially lower than any local work-function values actually present on the surface, coincident with an artificially reduced value for the fitted Richardson constant A [58]. Figure 8 shows the results of fitting simulated data from a model surface comparable with typical dispenser cathodes—a checkerboard consisting of only 2 and 4 eV. The fitted $\Phi = 1.57$ eV is smaller than either of them, with a fitted A much smaller than its conventional theoretical value.

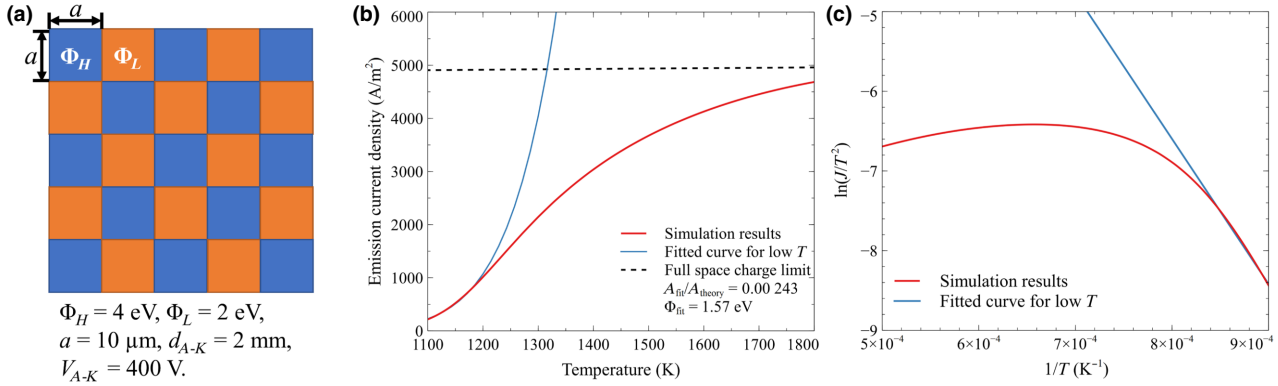

FIG. 8. Simulation and fitting of the thermionic emission from a heterogeneous cathode with a checkerboard work-function distribution. (a) The surface work-function distribution and anode setup. The surface consists of 10 μm patches with 4 eV and 2 eV local work functions. (b) The simulated current density, full space-charge-limited current density and fitted curve for low-temperature region, clearly showing a fitted work function (1.5 eV) much lower than any surface local work function, and a very small A (10^{-3} of the theoretical value). (c) The classical fitting procedure for the simulated emission current density by plotting ln(J/T^2) versus 1/T and linearly fitting the low-temperature part.

Given the uncertainty in A and in the applicability of the RLD form [Eq. (10)], there is significant uncertainty in the meaning of apparent work-function values extracted from fitting ln(J/T^2) versus 1/T data. This uncertainty is particularly significant when the emission behavior deviates from the RLD equation [i.e., ln(J/T^2) versus 1/T is not linear] and especially when the fitting leads to an A value differing from the conventional theoretical value by many orders of magnitude. The most objective conclusion to draw when RLD-data-fits imply a radically different A value from the conventional theoretical one is that the physics of the emission is not well-modeled by the simplified RLD equation and that the apparent work function therefore cannot be reliably identified as any particular local work function of an actual surface of the emitting material. There is clearly a need to develop more advanced models of emission physics to capture the non-RLD behavior and to understand the relationship between the measured emission current and the local work function(s) from heterogeneous thermionic cathode surfaces.

Given the above observations, it is often insufficient to report only a fitted apparent work function to evaluate the thermionic emission performance of a cathode. Specifically, when emitted current density data yield an anomalously low value for the extracted pre-exponential constant A, it generally means that the emission is limited by complex physics mentioned above, and the apparent work function is not a true work function of the surface and does not really capture the emission tendency. Consequently, the emission performance may not be very promising even if it shows an extremely low fitted Φ (e.g., <1 eV). Thus, we suggest that when discussing the thermionic emission behavior of a cathode by fitting the RLD equation, the fitted values of both A and Φ need to be reported. Alternatively, the anomalous value of the fitted A can be avoided by only fitting the work-function value with A equal to its theoretical value A_0 [59,60], especially at the temperature(s) of interest to the application. This approach was discussed by Hensley [60] as the *effective work-function* approach with the fitted Φ called the *effective work function* of an emitter. It provides a uniform scale to evaluate and compare the thermionic emission behavior of different cathodes.

Other thermionic emission measurement methods include the calorimetric method [48,49] and thermionic emission electron microscopy (ThEEM) [61,62]. Similar to PEEM, ThEEM is usually measured by applying a large electric field, so the patch-field effect may become negligible. In those cases, ThEEM can provide information on the spatial distribution of the work function on a cathode surface. However, typical ThEEM microscopes require the emission current to remain low enough to avoid space-charge distortion of the electron optics. Therefore, ThEEM measurements of work functions may need to be conducted at temperatures much lower than temperatures of practical application interest. If these practical applications rely on phenomena that change the emitting material surface conditions at high temperatures, the ThEEM-inferred values, while being correct for the temperatures at which they were measured, may not be the values associated with the higher temperature (higher emission current density) conditions of practical significance.

Similar to the case of thermionic emission, the work function can also be estimated from field-emission experiments [11]. In this scenario, the Fowler-Nordheim equation is the governing equation, which describes the emission current density from electrons tunneling through

the potential barrier on the surface [40,63]:

$$J_F = \frac{A}{k_B^2 c_f^2} \exp\left(-\frac{b_f}{F}\right), \tag{11.1}$$

where A is the same quantum mechanics-based constant present in the Richardson-Laue-Dushman equation, F is the applied electric field, and b_f and c_f are functions of work function and electric field given by following equations:

$$b_f = \frac{4}{3\hbar}\sqrt{2m\Phi^3}v\left(\frac{\sqrt{e^2F/4\pi\varepsilon_0}}{\Phi}\right), \tag{11.2}$$

$$c_f = \frac{2}{\hbar F}\sqrt{2m\Phi}t\left(\frac{\sqrt{e^2F/4\pi\varepsilon_0}}{\Phi}\right), \tag{11.3}$$

where the functions $v(y)$ and $t(y)$ above can be approximated by

$$v(y) \approx 0.936814 - y^2, \tag{11.4}$$

$$t(y) \approx 1 + 0.06489y + 0.0458308y^2, \tag{11.5}$$

and $y = \sqrt{e^2F/4\pi\varepsilon_0}/\Phi$ in these expressions.

Field-emission experiments are typically conducted with extremely high electric fields comparable to the image-charge potential (on the order of 10^9 V/m or 1 V/nm). Hence, the observed work function is the strong field local work function discussed in Sec. I A 2, where Schottky barrier lowering effect [Eq. (5)] is significant. Furthermore, this field is strong enough to overwhelm the patch field created by patches larger than a few nanometers and the patch-field averaging effect will likely not be observed in these experiments.

Similar to the case of empirically extracting the work function in thermionic emission experiments by fitting to RLD equations with Φ (and perhaps A) as fitting parameter(s), the work function can again be inferred by empirically fitting the Fowler-Nordheim equation to the field-emission data. However, in practice, there are often significant challenges with this approach.

First, all the issues discussed above for fitting the RLD equation, except those due to patch fields, exist in fitting the Fowler-Nordheim equation to field-emission data, including the uncertainty in the appropriate value of A. In addition, field emitters are likely to have extremely sharp geometry to enhance the local electric field, which could significantly complicate the relationship between the emission current density, the effective emission area and the applied electric field. For example, the current density is obtained by dividing the measured emission current by the assumed emission area. However, the strong electric fields required for field emission typically result from field-enhancing sharp tips, including often unknown microscopically sharp morphological features on the surface with high geometric aspect ratios. This makes it difficult to accurately know the emission area and to precisely infer the work function from the measured emission current versus externally applied voltage data [64]. Furthermore, when measuring sufficiently high current densities, space charge will also play a role in distorting the Fowler-Nordheim-type emission current [65–68].

The work function could be measured through other approaches if it is involved in the related physics. For example, in a low-energy electron microscopy (LEEM) experiment, the sample's work function could be measured by acquiring the transition voltage between the mirror mode and scattering mode with proper correction from the electron gun's work function, because such a voltage suggests the minimum energy for an incident electron starting to interact with the material's electrons, exactly matching the work-function definition [69,70]. Again, since the technique is based on the microscopic method with high extraction field, it is able to directly resolve the local work function as the patch-field effect has been overcome.

III. WORK-FUNCTION PREDICTION WITH THEORETICAL, COMPUTATIONAL, AND DATA-CENTRIC APPROACHES

Besides direct experimental measurements of work function, it is also useful to develop mature approaches to calculate the work function via computational tools. Computational predictive models not only enable relatively fast exploration of the work-function values of different materials, but also deepen understanding of the relationship between work function and other physical properties such as composition, structure, and surface chemistry. Historically, physics-model-based methods such as the free electron gas model and jellium model are used to calculate the work function of simple metal systems. More recently, with the rise of computational science and the development of density-functional theory (DFT), DFT-based work function calculation has become the primary method to calculate work functions and has enabled expansion of theoretical predictions to more complex systems, such as oxides, borides, nitrides, organic compounds, and low-dimensional materials.

A. Pre-DFT methods for calculating work function

In the mid-20th century, prior to the development of modern digital computation, the work function was calculated using simplified analytic theoretical models. Several early works assumed a free electron gas (Sommerfeld) model to calculate the work functions of metals, using the early understanding of metals with electron occupations represented with a Fermi-Dirac distribution. Wigner and Bardeen summed up the energy terms of the electrons

and ions of a metal, and compared the energy difference between a metal system with its missing-electron counterpart to calculate the work function of alkali metals [71]. Later, Bardeen included the effect of the dipole layer on the surface to further modify the assumed free electron gas model, and successfully reproduced the measured work function of alkali metals [72]. These early efforts provided relatively accurate calculated work functions for alkali metals compared to experimental values, with a typical error of 0.05 to 0.2 eV.

Further development on the use of analytic models to calculate the work function included the jellium model (uniform electron model) where the positive charge from the nuclei was considered as being uniformly distributed, and the near-surface dipole from electron-cloud spreading and smoothing (as discussed by Smoluchowski [9]), and the image-charge effect were taken into account. In 1971, Lang and Kohn went further by including a pseudopotential of the nuclei, enabling the calculation of the work functions for various crystal surfaces [12]. They provided relatively accurate predictions of work functions of simple metals, including alkali and alkaline earth metals as well as Al, Pb, and Zn, within approximately 0.2 eV compared to experimentally measured polycrystalline values. However, their predictions significantly underestimated the work functions of noble metals by approximately 1.5 eV due to the complex *d*-electron behavior. Following that, Russier and Badiali further advanced the approach in 1989 by including the *d*-band and *s*-band hybridization, resulting in more accurate calculation results, especially for noble metals, such as Ag, with errors smaller than 0.1 eV [73].

Despite the pioneering success of these methods, significant limitations remain. At the time these analytic methods were developed, the computational capabilities of the time were limited in the ability to numerically evaluate the resulting expressions, hindering any extensive systematic exploration. More significantly, these models were only reasonably accurate for simple material systems, i.e., free electron metals. For more chemically complex material systems such as oxides, organic compounds, materials with surface adsorbates, or low-dimensional materials, these traditional methods were not able to capture the actual charge distributions and therefore the work functions. The advent of quantum mechanical computational methods like DFT have enabled researchers to circumvent these limitations, as discussed in the next section.

B. Work-function calculation with DFT

1. Introduction and technical aspects of DFT work-function prediction

The vast increase in computational power since the 1990s has made it possible to directly predict the work function of a material surface via quantum mechanics-based atomistic calculations. In solid-state materials science, the most widely used quantum mechanical modeling method is DFT, based on the Nobel prize-winning development by Pierre Hohenberg, Walter Kohn, and John Pople that the ground-state energy is a functional of the electron density [74]. Use of the correct electron density minimizes the energy functional, enabling DFT to predict the electronic structures of many-body systems by considering the (vastly) simpler case of single electron wave functions that interact with the total electron density. In this way, DFT not only gives the correct bulk electronic structures and densities of states, but also correctly captures the average electrostatic potential of electrons in the materials. Therefore, DFT can be used to calculate the Fermi level and the vacuum level away from a terminating surface, thus yielding the work function. In contrast to the traditional analytic theoretical models discussed above, DFT is an atomistic calculation method, where the position and type of every atom under investigation can be specified. Therefore, detailed examinations of different material composition, structure, and surface termination and chemistry can be systematically evaluated, yielding a much deeper understanding and insight compared to using only analytic physical theory models. Some examples of DFT work-function calculations are shown in Fig. 9.

DFT calculations of work functions of bulk material surfaces typically use periodic boundary conditions and a slab geometry, consisting of a section of the bulk material cleaved along a specific crystal plane. The termination of interest is thus exposed, and a vacuum region is introduced into the simulation cell. With periodic boundary conditions, the cell is repeated three dimensionally to form material slabs separated by vacuum regions. The Fermi level is directly output from the DFT-calculated electronic structure. The DFT calculation also provides the electrostatic potential for each point in space of the system, which can be used to calculate the converged planar-averaged electrostatic potential along the direction normal to the surface of interest. This converged electrostatic potential value away from the surface is taken as the local vacuum level. The work function is computed as the difference between the Fermi level (which is directly output from any DFT calculation) and this local vacuum level.

Similar to performing DFT calculations of other material properties, obtaining an accurate work-function value requires parametric convergence tests. In slab calculations, this includes convergence of the cutoff energy of the plane-wave basis set and *k*-point mesh, slab thickness, number of surface layers relaxed, and vacuum region thickness. Regarding the effect of slab thickness in particular, Fall *et al*., studied the oscillation of calculated work functions of thin metal slabs resulting from quantum size effects, and formulated a postprocessing method based on macroscopic potential averaging, which effectively reduces such size effects, enhancing the convergence of work function with slab thickness and enabling more computationally efficient

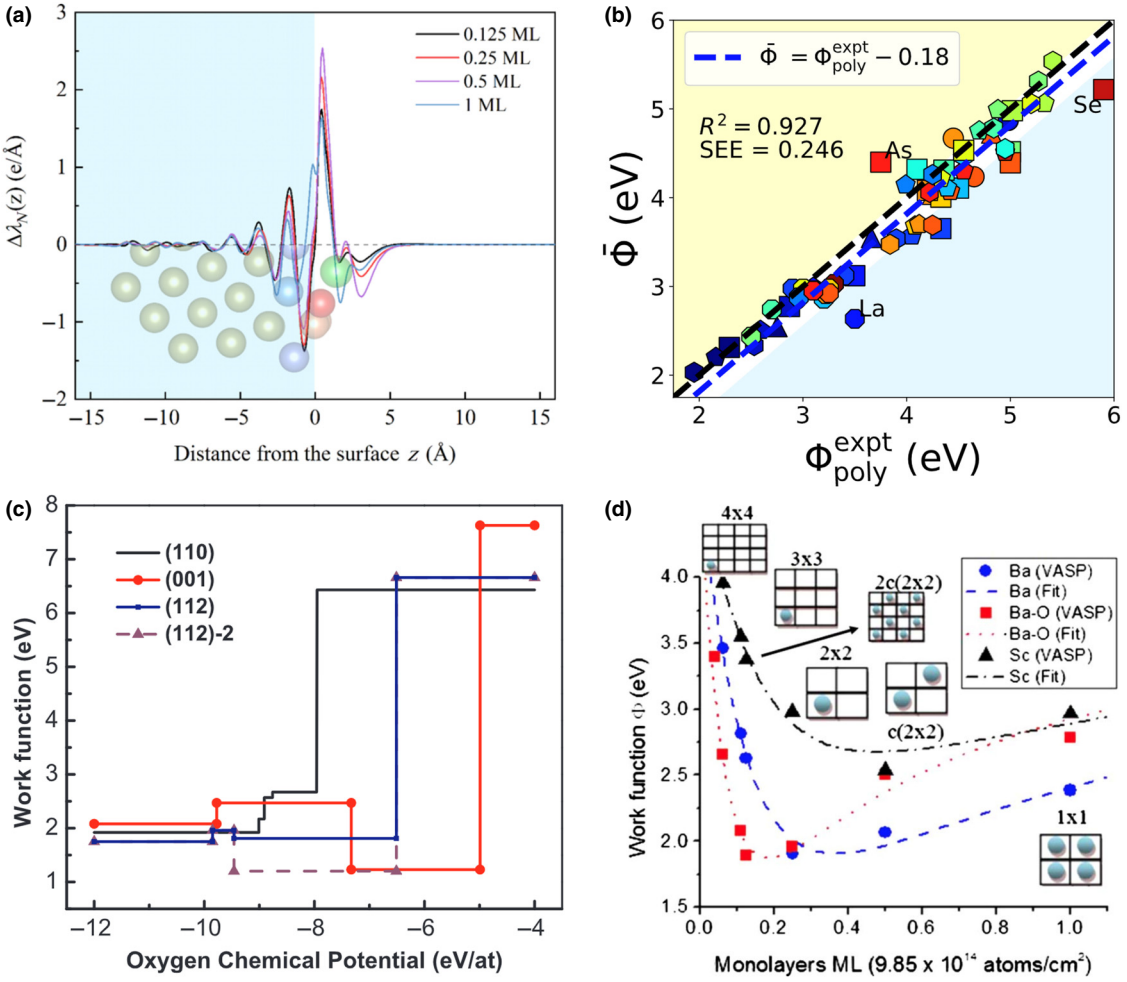

FIG. 9. Examples of DFT work-function calculations. (a) Charge-density differences of Ba_xO coated on Hf $(10\bar{1}2)$ surface with different Ba coverage, which is closely related to surface dipole and work function (from Ref. [75], Copyright © 2022 American Chemical Society). (b) Comparison of DFT calculated area-weighted average work function versus their experimental measured counterparts of elemental polycrystals, suggesting consistent prediction with a constant underestimation of the work function of about 0.24 eV (from Ref. [76], Copyright 2019, with permission from Elsevier). (c) The impact of chemical environment on work function of different W surface facets. The stable configurations change with O chemical potential (from Ref. [77], Copyright 2018, with permission from Elsevier). (d) The DFT calculated work-function variation with coverage of different Ba, Sc, and Ba-O dipoles on W(001) (from Ref. [78], Copyright © 2010 American Physical Society).

DFT simulations with slabs comprising fewer layers to reach convergence [79]. The calculation parameter values resulting in converged work-function results are case dependent. As a general rule of thumb, it is typically sufficient to have a vacuum region that is 15–20 Å thick, a material slab that contains order approximately 10 repeat units, and a relaxed, near-surface region of the slab that is 1–2 repeat units thick. However, cases with long-range interactions, e.g., dipole or strain effects, may require significantly thicker slabs, and some systems may not show stable convergence for a computationally tractable supercell size. For instance, Lee *et al.* showed that the wide band-gap insulator $LaAlO_3$ does not contain a bulklike region with converged electrostatic potential along the direction perpendicular to the (001) surfaces, even when the slab thickness has reached 16 layers (approximately 29 Å). In fact, Lee *et al.* estimated it would take 26 layers before convergence was obtained. This effect is due to the large surface dipole on the perovskite (001) surfaces, together with $LaAlO_3$ being an insulator, making it more difficult to obtain a converged work function than for a metallic material due to longer Debye (electron screening) lengths in the insulator [80].

2. Accuracy of DFT calculated work function

DFT has been used to calculate the work functions of many kinds of materials, including pure elements [76,81], metal hexaborides [82,83], transition metal carbides and oxides [10,84–86], and two-dimensional (2D) materials

like graphene and MXenes [87–90], among others. Some recent studies have benchmarked the accuracy of DFT calculated work functions against available experimental data, and in this section we discuss the results of these benchmarking studies.

For elemental crystals, De Waele *et al*. [81] compared experimental work-function values of polycrystalline metals to the lowest DFT-calculated value among different surface terminations for each metal, and found that DFT calculations performed using the local density approximation (LDA) and the more physically complex generalized gradient approximation (GGA) yield accurate work functions with errors generally below 0.3 eV, though it should be noted that LDA yields better overall agreement with experiment (at least for metals), while GGA tends to show a systematic underestimation of the true work function. Tran *et al*. [76] proposed an area-weighted DFT-GGA work function based on the Wulff shape with values that compared well with experimental polycrystalline data with a mean absolute error of 0.24 eV. In both studies the DFT-calculated work functions were consistently lower than experimental values. These two studies obtained errors between experiment and DFT that were nearly the same, despite the use of the lowest work function value in De Waele *et al*. and the area-weighted average by Tran *et al*. This is consistent with the fact that the work-function variation between different surface terminations for metals is quite small, generally within approximately 0.2 eV [91].

More targeted DFT studies of tungsten and hafnium with various surface orientations and adsorbate types by Vlahos *et al*. [78], Jacobs *et al*. [92], Zhou *et al*. [77], and Bai *et al*. [75] demonstrated qualitative agreement between calculated DFT work functions and experimentally derived work functions from thermionic emission experiments. However, such comparisons are less reliable than the case of clean metals, because, unlike clean metals, the surface of thermionic dispenser cathodes is structurally and chemically complex, and the precise coverage and structure of the adsorbates, especially at the typical high operating temperatures, is not rigorously known [93].

For compound materials, Uijttewaal *et al*. [82] and Schmidt *et al*. [83] have demonstrated reasonably good agreement between DFT-GGA calculated work functions and experimental values for metallic lanthanum hexaboride (LaB_6) for different surfaces [94], with errors on the order of 0.1 to 0.5 eV. A recent study from Chambers and Sushko [86] carefully controlled $SrTiO_3$ terminations and calculated corresponding work functions using DFT, where the results showed quite satisfactory agreement between DFT and angle-integrated ultraviolet photoelectron spectroscopy (UPS) measurements on TiO_2 termination, differing by less than 0.3 eV. There is a relatively large deviation between the experimental and calculated SrO-terminated work functions (about 1 eV) likely due to the Sr vacancies. Another work from Ma *et al*. [14] performed a case study on $SrTiO_3$ using experimental data where work function and surface structure were studied together. This work included careful comparisons between hybrid functional Heyd-Scuseria-Ernzerhof (HSE) DFT-calculated work functions and experimental values of the same surfaces, showing an average difference between DFT and experiment of about 0.2 eV, the same level of accuracy as elemental materials. In the work of Ma *et al*. [14], it was also demonstrated that hybrid functionals like HSE are needed to predict accurate work functions for semiconductors and insulators, since semilocal functionals like GGA do not give correct VBM and CBM energy levels simultaneously, due to the underestimation of the band gap. However, it was found that GGA can typically predict *relative* work functions almost as accurately as HSE, for example, between different surface terminations, and is thus often suitable to more quickly calculate the influence of surface adsorbates, terminations, or other effects of surface modifications on the work function.

Overall, these studies on pure elements [76,81], compounds [82,83], decorated surfaces [77,78,92], and complex oxides [14,86] all indicate that modern DFT-based methods, when used carefully, provide reliable work-function predictions compared to experimental values, typically within 0.2–0.3 eV for most cases.

3. Advantages and disadvantages of DFT work-function prediction

A key challenge of obtaining DFT-calculated work functions of chemically complex systems is knowing the precise surface structure that is present in the corresponding experimental or application conditions. For chemically complex systems, the work function is often highly dependent on surface terminations [10,85], reconstructions [95–99], and the presence of adsorbate species, such as O_2, CO_2, H_2O, etc. In addition, experimental samples often have defects and/or reconstructions, which, along with adsorbates, are sensitive to the material-preparation process and difficult to characterize at the atomic level [14]. Thus, it is often difficult to know at the atomic level what surface was experimentally measured and ensure that the same surface was precisely modeled with DFT. This can make comparison of work functions between experiment and theory difficult and uncertain.

On the other hand, the fact that DFT allows for controlling the position of every atom being studied opens the door to understanding trends and factors influencing the work function in ways that are not possible with experiment. For example, introducing defects, modifying composition, placing adsorbates on the surface, changing surface orientation and termination, and adding strain are straightforward to implement in DFT calculations, making it possible to systematically investigate the influence

of these and other relevant factors on the work function [14,84,85].

Other materials properties obtainable from DFT calculations can also be used to further understand the work-function physics of different classes of materials. As a concrete example, recent DFT studies on perovskite oxides demonstrated a linear correlation between the work function and the bulk O 2*p* band center [100]. The O 2*p* band center is defined as the centroid of the O atom component of the projected density of states. The O 2*p* band center is a bulk electronic structure descriptor, which serves as a proxy to estimate the work-function value and is much faster and easier to obtain than an explicit work-function calculation. A similar correlation is also observed in the calculated work function of two-dimensional MXene materials decorated with organic adsorbates, where the O 2*p* band center of the adsorbate molecule controls the work function [90]. Using bulk-calculation-based descriptors of the work function, such as the O 2*p* band center, not only provides a method of understanding work-function trends, but also opens up the opportunity for more efficient work-function predictions based on high-throughput DFT screening studies and data-centric approaches. Recent work from Ma *et al.* used the correlation of work function with the bulk O 2*p* band center to screen more than 2000 perovskite oxide materials in search of potentially low work-function materials. They not only found a handful of potential perovskite compositions that contain specific surfaces with low work functions of 2 eV or less, but also provided key design guidance toward understanding which perovskites should exhibit low versus high work functions based on the electron count of the transition metal in the perovskite *B* site, where transition metals with few electrons (e.g., one or two *d*-shell electrons) have low work functions while those with mostly filled *d* shells have high work functions [100].

DFT can provide mechanistic understanding of the role of the work function in different technological applications. For example, DFT has been used to find the most stable surfaces and corresponding origin of low work functions of tungsten-based thermionic dispenser cathodes under typical operating conditions [77,92]. Another study systematically evaluated the modulation of the work function of tungsten covered with a monolayer of a variety of atoms using DFT, and successfully explained the observed work-function trends being due to strain and surface dipole [101]. In solar photovoltaic applications, knowledge of the work function is needed to assess electronic band offsets (i.e., band alignment) between different material layers comprising the solar cell, which determine the efficiency of charge transport in the device. Halide perovskite materials such as methylammonium lead iodide ($CH_3NH_3PbI_3$) have undergone a meteoric rise in photovoltaic performance over the past decade. DFT has been used to study the work function and energy-level alignment of the methylammonium-terminated and PbI-terminated surfaces with other interfacial layers to understand and explain experimental observations of cell performance [102]. Finally, as an example from catalysis, DFT is used in conjunction with XPS measurements to compare water reactivity of different $LaFeO_3$ surface terminations, and investigate possible intermediate species, providing helpful insight for the design of catalyst materials [103].

Despite the large increase in computational power over time, the size of the surface slab usable in DFT calculations is still relatively small, usually no more than a few hundred atoms with a slab surface area smaller than a few nm^2. Due to the limited size of the simulation cell, DFT cannot directly accommodate defects at low coverage or concentration, surface features with long periodicity, or disordered, extended structural domains, although in some cases one may be able to extrapolate to the dilute limit the concentration dependence of the work function based on smaller simulation cells where the coverage or defect density is high. Also, there may be additional complexities or issues when introducing strong electron donors or acceptors into the DFT simulation cell. As an example, we consider Nb-doped $SrTiO_3$ (Nb:STO). Pure stoichiometric Nb:STO is an *n*-type semiconductor as Nb dopes extra electrons into the system. However, after introducing O adsorbates to the surface of a typical DFT slab calculation, the system can become an insulator if the oxygen accepts more electrons than the Nb donates. This effect can easily occur with modest Nb doping and a significant surface coverage of oxygen because the surface slab in DFT is small and the absolute number of electrons donated by Nb is small. Therefore, O easily drains electrons from Nb:STO. In actual experiments, the density of donated electrons in the bulk of Nb:STO overwhelms the small surface area containing O adsorbates, and thus maintains its *n*-type character. If the electron donor or acceptor is on the surface, it may form a surface dipole and thus create an electric field across the slab and between periodic images of the simulated slab, which may result in shifts to the electrostatic potential [80] or large changes to the electronic structure, such as metallization of a semiconductor or an insulator. To avoid such artifacts, DFT dipole corrections can be used, and a structurally symmetric slab, which contains the same surface species on both sides is often preferred as the dipoles will cancel each other. For calculations with charged defects and/or adsorbates, a background charge of opposite sign is introduced to the system to avoid divergent Coulomb energy. Such artificial charges are also repeated via periodic boundary conditions, and the interaction between them has an erroneous influence on both the total energy and the one-electron eigenvalues and eigenstates. Therefore, a correction is needed, especially for the slab calculations as the artificial counter charge may induce spurious states in the vacuum. A recent study devised a self-consistent potential correction method

addressing this issue [104], and this correction has been implemented into the Vienna *ab initio* simulation package (VASP), one of the most popular DFT code packages.

C. Data-centric approaches to predict the work function

In addition to theoretical and computational approaches to calculate the work function, there have been a number of recent studies employing data-centric machine-learning methods to predict the work function.

The simplest work-function values to predict are those of elemental metals. Li *et al*. [105] tested a series of regression models in predicting values of 59 elemental work functions comprising five alkali earth metals, 37 transition metals, and 17 rare earth metals. They built their models using only the mechanical properties of Young's modulus, bulk modulus, and shear modulus as features, and found that the extreme gradient boosting (XGBoost) model produced the best work-function estimate from fivefold random cross validation with a root-mean-square error (RMSE) of about 40 meV. This low error on test set data illustrates the strong physical connection between mechanical properties and work function, which is discussed in more detail in Sec. IV D.

Another example of predicting work function using data-centric approaches comes from Xiong *et al.*, [106] who used machine learning to build random forest regression models to separately predict the work function of (001) AO- and BO_2-terminated perovskite oxides. The machine-learning models in their work used features based on the elemental properties comprising each composition under study, and also contained a handful of DFT-calculated electronic structure descriptors, including the O 2*p* band center. Their models had an average root-mean-square error of about 0.5 eV for materials with a work function spanning a range of about 9 eV, indicating these models are likely of qualitative utility to estimate the work-function magnitude but are currently unable to provide quantitative prediction of the work function. Interestingly, by analyzing the relative significance of each of the features used in their random forest models, they found that the O 2*p* band center was the most useful feature for predicting the work function of BO_2-terminated perovskites. On the other hand, the *s*- and *d*-valence orbital radii of the *A*-site element were the most helpful features for predicting the work function of AO-terminated perovskites, with the O 2*p* band center being the fourth most useful feature. These findings are broadly in agreement with the qualitative arguments made by Jacobs *et al.* in understanding the relevance of electronic band levels and thus the O 2*p* band center, the dominant factor for setting the BO_2-terminated work function, versus the role of surface dipoles, which is the dominant factor for setting the AO-terminated work function. Despite being largely governed by the surface dipole, the bulk electronic structure, and O 2*p* band center still play a sizable role in setting the work function of the AO-terminated surface.

The work of Hashimoto *et al*. [107] sought to conduct a Bayesian optimization-based active learning campaign to screen through the Materials Project database in search of materials with very low and very high work-function values. To accomplish this, they fit a Gaussian process regression model to a set of elemental features of the bulk material composition, and used this model to predict an approximate "bulk work function," which is obtained from the Fermi level of a bulk DFT calculation. Their work resulted in low work-function materials like Cs (110) and high work-function oxides like $KEuO_2(111)$. These extremal cases make physical sense, indicating their model is at least qualitatively useful. However, reliance on predicting the approximate bulk work function does not capture the complex surface-dipole physics critical to obtaining accurate work functions for many materials. Because of this, there are instances where the model predictions and calculated work-function values have discrepancies of several eV, indicating a failure of the model relying on bulk features to screen work function for a wide range of material chemistries. As a specific example, the material $LiEuO_2$ has an approximate bulk work function of 11.2 eV, but slab work functions range from 3.9–5.4 eV.

A drawback of the work of Xiong *et al*. and Hashimoto *et al*. is the reliance on predicting the work function, a property of a specific material surface, using only features comprising the bulk composition of the material. For this reason, separate models typically need to be made to predict work functions of different surfaces or different structural families or chemistries of materials. For example, the work of Xiong *et al*. focused exclusively on work functions of perovskite oxides, and built separate models to predict the work functions for AO- and BO_2-terminated perovskite surfaces. A more sophisticated model of work function was developed recently by Schindler *et al*. [108]. In this work, the goal was to develop a machine-learning model capable to predict the work function of a wide range of material chemistries, and predict the work functions of different surface orientations for a particular composition. To do this, Schindler *et al*. first conducted a suite of high-throughput DFT calculations at the Perdew-Burke-Ernzerhof (PBE) level totaling more than 23 000 surface slab simulations for nearly 2500 unique materials compositions comprising unary, binary, and ternary materials. Initial benchmark tests using a large number of elemental property features of the bulk materials showed a large tenfold cross-validation mean absolute error of 0.79 eV. Focusing the feature generation to just the near-surface region resulted in slightly reduced errors of 0.61–0.64 eV, depending on the exact method employed. However, by (1) using physically motivated features based on *a priori* knowledge of previous works, which found a strong

connection of electronegativity and atomic size to work function [109], and (2) a surface-sensitive featurization technique, which used the minimum, maximum, and average of the electronegativity, size, first ionization energy and Mendeleev number of the top three atomic layers of each surface, they found that a random forest model produced tenfold cross-validation mean absolute errors of about 0.19 eV, within the established range of DFT error of 0.3 eV. While understandable from the standpoint of needing to calculate a large database of work function values, it is worth pointing out that this machine-learning model has about a 0.2-eV mean absolute error relative to DFT-PBE values, and for materials, such as semiconductors and insulators, the PBE value of work function may still differ significantly from the true experimental value, for the reasons discussed in Sec. III B 2.

Overall, the use of machine-learning approaches for predicting work functions remains in the nascent stage. We believe there are opportunities to formulate improved models to predict work function. One path that could yield more powerful models is the use of more complete features based on the structure of a surface slab as input. Models with full structural awareness may be able to discern the impacts of different bulk structures, e.g., distinguishing values for different polymorphs. Such approaches might also be able to treat the complex surface-dipole physics, which strongly influences the work-function values of ionic materials like oxides, enabling more nuanced prediction of the work function of different surface terminations for a particular material. Many sophisticated machine-learning models that allow for featurization of structure now exist, e.g., graph-based neural-network approaches [110,111]. In addition, as the work function can be separated into a bulk component and a surface component, there may be approaches, which employ machine learning to separately learn key features controlling the bulk electronic structure and the surface-dipole physics, then combine the separate bulk and surface component predictions into a work-function prediction for a specific material surface. In sum, a key challenge in this space is how to engineer a set of features, which is sufficiently complex as to capture the rich work-function physics across materials chemistries and surface orientations and terminations, yet simple enough to be readily calculable, thus producing substantial time and cost savings compared to performing a DFT calculation or experiment to obtain the work function.

IV. APPLICATIONS OF WORK FUNCTION AND ENERGY-LEVEL ALIGNMENT ENGINEERING

The basis of many modern technologies relies on moving electrons from a material to vacuum or from one material to another, and the alignment of the relative energy levels is essential to such processes. Because the work function gives the energy between the local vacuum energy level and the Fermi level, and because this local vacuum energy level might be directly of relevance or shared between the two surfaces in some approximation, the work function typically provides a benchmark for the energy-level alignment. More specifically, such alignment might be between a solid phase and vacuum, e.g., as in electron emission, in which case the work function of the solid gives direct information about the relative energy levels of material and vacuum. Such an alignment may also exist between two condensed phases, which is referred to as band alignment. In this scenario, the electrons do not travel through vacuum, so the work function is not directly involved. Therefore, if changes from free surface dipoles to interfacial dipole are modest compared to the relative work functions, the relative work functions serve as a useful band-alignment guide at the interface. Additionally, the work function of a solid could also provide its relative energy level compared to standard redox potential or specific molecular orbital levels, e.g., the oxygen-reduction reaction. Thus, the relative work functions play a critical role in many technologies where electrons must be moved effectively between materials. These applications include electron emission, solid-state electronics, and electrocatalysis, to name a few. Some of these applications with the role of the work function illustrated are summarized in Fig. 10.

A. Electron emitters

One direct application of work-function engineering is electron emission, the case where electrons move from a material surface into vacuum. This scenario can be thought of aligning the energy levels between a solid-state cathode material and its adjacent vacuum, where the work function of the cathode serves as an energy barrier for the emitting electrons, and thus directly relates to the emission performance (i.e., emitted current density at a particular operating temperature and applied potential) of the cathode.

Depending on the mechanism of electron emission, an electron emitter could be attributed to one or a combination of the following types—thermionic (hot), field (cold), or photoemission cathodes [40,112]. As discussed in Sec. II C, the emission current density is commonly predicted using the RLD equation [Eq. (10)] for thermionic emitters operating in the temperature-limited regime, while for field emitters, the emission current density is described by the Fowler-Nordheim equation [Eq. (11.1)] [40]. There is also a category of cathodes called Schottky emitters, which uses a mixture of thermionic and field-emission mechanisms [40]. For photocathodes [40], Einstein's photoelectric equation [Eq. (7)] indicates that photoemission will only be enabled when the work function of the cathode Φ is smaller than the incident photon energy $h\nu$, and

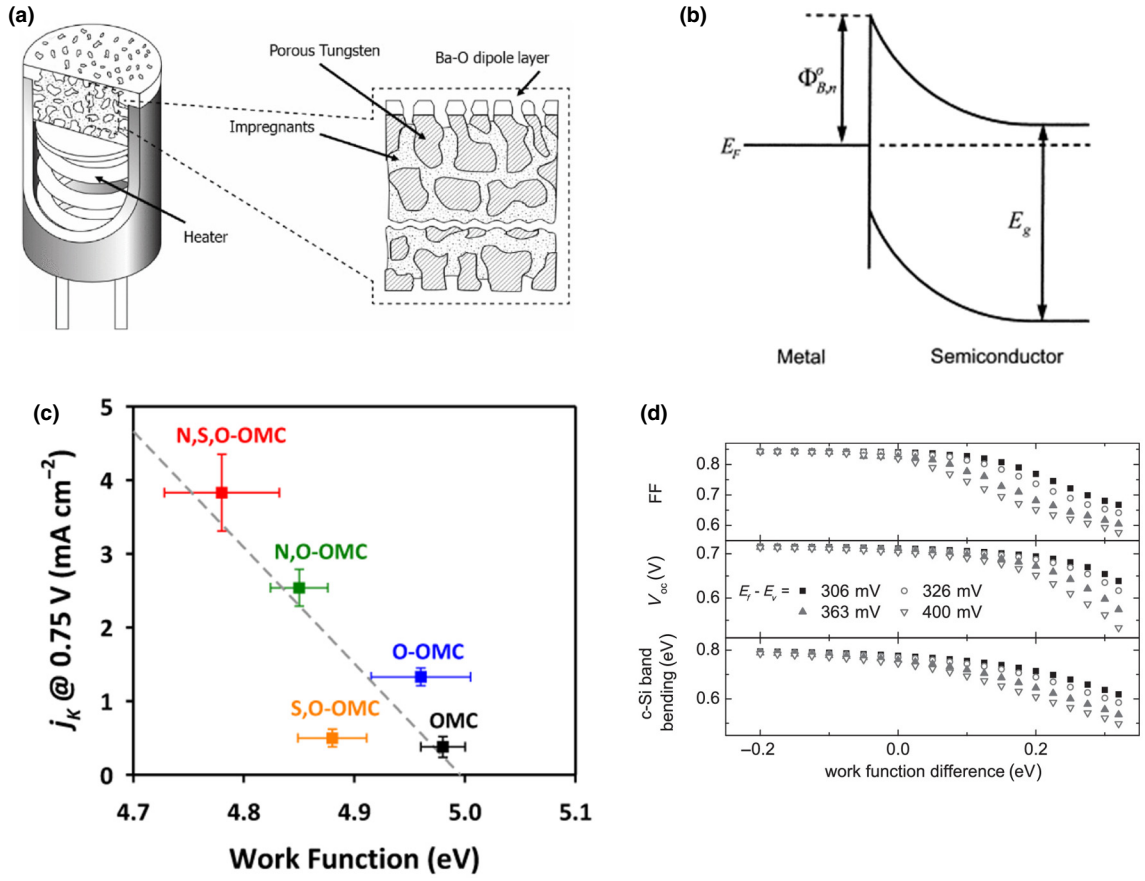

FIG. 10. Some applications of work-function engineering. (a) Schematic structure of dispenser B-type thermionic cathode (©2018 IEEE. Reprinted, with permission, from Ref. [112]), showing the surface BaO dipole layer that decreases the work function. (b) Schematic band diagram of a metal-insulator barrier, showing the work-function-related Schottky barrier at the interface (reprinted from Ref. [113], Copyright 2001, with permission from Elsevier). (c) ORR reaction current density as a function of the catalyst's work function (reprinted with permission from Ref. [114]. Copyright 2014 American Chemical Society). (d) DFT-simulated solar-cell parameters as a function of the work-function difference between the TCO electrode and the (*p*)*a*-Si:H layer for different distances of the Fermi level from the valence band (reprinted from Ref. [115], with the permission of AIP Publishing).

the quantum efficiency is approximately proportional to $(h\nu - \Phi)^2$. Therefore, a small decrease in emitter work function will lead to a dramatic boost in emitted current for all cathode types mentioned above.

Many different types of cathodes have been developed for emission applications. For photocathodes used for generating electron beams in radiofrequency applications, such as linear accelerators, free electron lasers, and related devices [40], people are pursuing low work-function-coating materials to boost the device performance, e.g., an alkali metal, such as Cs, coated on GaAs or GaN, which could lead to a work-function reduction of 2–3 eV compared to the uncoated material [116–119]. For field emitters used as cold cathodes in vacuum electron tubes, electron-beam lithography, and electron microscopes, one common method that has been developed is the introduction of materials with "sharp-tip" shapes, such as sharp-tip tungsten cold cathodes, arrayed emitters such as Spindt arrays as well as carbon nanotubes, to enhance the local electric field [33,40]. In addition to geometrical (e.g., sharp tip) and morphological (e.g., Spindt array) engineering of field emitters, the field-emission current densities can be further enhanced by applying a low work-function material or coating. Zhang *et al*. [120] and Nakamoto *et al*. [121] have fabricated field emitters using low work function LaB_6 (2.7 eV, compared to Mo- or W-based field emitter with an approximately 5 eV work function). Nakamoto *et al*. [122] have also employed TiN (3.2 eV work function) coating on Ni field-emitter array to pursue higher emission. Recently, there has been significant research on negative electron affinity (NEA) semiconductors derived from diamond and nitrides [123–125]. These NEA materials have been investigated for applications in photocathodes and field-emitter cathodes by proper energy-level pinning to facilitate the emission [123,126,127]. As a canonical NEA material, diamond realizes its NEA property from adsorption of H on the emitting surface. While the NEA property results in spontaneous electron emission of

conduction electrons in the diamond emitter, the wide band gap, and thus electrically insulating nature of diamond makes realization of current densities sufficient for many functional applications difficult to achieve, thus motivating the development of alternative methods of realizing NEA materials capable of producing high emitted current densities. Very recently, researchers have created a photoemission cathode, which realizes an effective NEA state using optically pumped hot electrons. These so-called hot electron laser-assisted cathode devices comprise a semiconductor-insulator-metal (e.g., Si-SiO_2-graphene) heterostructure where the electrons originate from the semiconductor material, which does not need to have a low work function. By combining photoexcitation (from an incident laser) with an applied bias potential gradient, the electrons are excited into the semiconductor conduction band, tunnel through the insulating layer and then emit from the metal layer. In the example of a Si-SiO_2-graphene device, graphene has a high work function of over 4 eV, but the applied bias and band alignment of the device creates an effective NEA material because the hot electrons from the semiconductor reside above the graphene vacuum level after tunneling through the SiO_2 layer, resulting in strong spontaneous emission. This NEA property is mainly the result of band-alignment engineering as opposed to surface chemistry modification (e.g., with H adsorption on diamond), and opens the door to experimenting with an array of different semiconductor-insulator-metal combinations together with surface and interfacial engineering [128,129].

For thermionic emitters that are widely used as electron sources of electron microscopy, electron-beam lithography, and high-frequency vacuum electronic devices, the main research efforts have been devoted to lowering the cathode work function and improving the operational stability and longevity. Besides some early works on less-stable oxide cathodes [130–132], the mostly studied and commercialized materials are hexaborides [133–135], tungsten-based dispenser cathodes [136,137] and scandate dispenser cathodes [112]. Hexaborides have moderately low work functions of approximately 2.5 eV created by an intrinsically polar surface. Dispenser cathodes, on the other hand, are able to achieve apparent work functions (extracted from thermionic emission current measurements, see Sec. II C) of about 2 eV owing to the vaporization of the Ba-containing impregnates and the adsorption of Ba-O monolayer species that creates a large surface dipole. However, dispenser cathodes generally suffer from lifetime and contamination issues due to the volatile nature of the impregnate species [112,138–142]. In the past two decades, a subgroup of dispenser cathodes containing Sc_2O_3 nanoparticles in the W matrix (or the impregnate), commonly known as scandate cathodes, has drawn great attention in both research and industrial applications, due to the lower apparent work function (about 1.5 eV) and higher beam brightness of these cathodes compared to nonscandate dispenser cathodes. However, scandate cathodes also have emission uniformity, performance and manufacturing reliability issues, and the mechanism of the lower apparent work function still remains unresolved, though understanding has improved in the past few years [77,143,144]. Recently, researchers have proposed using stable oxides with polar surfaces to obtain low work-function emitters [10,100,145]. A key area of current and future research is the development of next-generation thermionic emitters with low work function, long lifetime, and low volatility.

B. Solid-state electronic interfaces

The work function is a crucial property to understand the electrical properties of material interfaces in solid-state electronics [146]. When two different materials are brought into contact, thermodynamic equilibrium will align the Fermi levels of the two materials at the same energy, as the Fermi level is the chemical potential of electrons in the material. Thus, if the two materials have different work functions, electrons will flow from the lower work-function material to the higher one, leading to several effects at the interface.

Taking a metal-semiconductor interface as an example, the electron flow will cause each material to become slightly biased, where excess charge would primarily accumulate on the semiconductor side near the interface because of its relatively lower (compared to the metal) electrical conductivity, causing the formation of a space-charge region and band bending [146]. Meanwhile, this charge flow will form an energy barrier at the interface due to the contact potential difference. For the contact of a metal and an *n*-type semiconductor, as shown in Fig. 10(b), if the work function of the metal is larger than the work function of the semiconductor, the metal-semiconductor junction will be rectifying, and there will be a sharp energy barrier on the interface, known as a Schottky barrier. In the idealized case, its height (denoted as Φ_{bn}) is determined by the metal work function Φ_M and the semiconductor electron affinity χ, according to the Schottky-Mott rule:

$$\Phi_{\mathrm{bn}} = \Phi_M - \chi. \tag{12}$$

On the other hand, if the metal work function is smaller than the (*n*-type) semiconductor work function, the interface region will be nonrectifying, leading to the formation of an Ohmic contact.

The above Schottky-Mott rule [Eq. (12)] and associated models for rectifying and Ohmic junctions are the simplest, ideal cases. In reality, defects and imperfect bonding at the interface (e.g., dangling bonds) lead to charged interface states, which can pin the Fermi level and cause the true Schottky barrier height to deviate from

the ideal case value. This makes the barrier height calculation significantly more complicated. Several theoretical treatments have been developed to deal with the deviation of the Schottky barrier height from the theoretical prediction of Eq. (12). For example, Freeoff and Woodall have developed an effective work-function model, which substitutes the metal work function in Eq. (12) with a proper weighted average work function of different interface phases ("effective work function", note this term is different from the one previously mentioned in Sec. II C, since they were discussed by different researchers in different scenarios). Schmitz *et al*. studied the Schottky barrier between *n*-type GaN and various metals, suggesting that the barrier height indeed increases monotonically with increasing metal work functions, although the value does not scale proportionally. These studies suggest that despite the additional complexity induced by sometimes sophisticated interfacial chemistry, the relative work functions of the metal and the semiconductor are still relevant to the rectifying nature and the Schottky barrier height [147,148].

The correlation between the work function and the interfacial barrier height directly relates to device properties, such as charge transport across the interface. Specifically, despite the possible complex interfacial physics (which may cause very weak dependence between work functions and barrier height), tuning the work functions of both sides of the interface is still a useful approach to achieve optimum barrier height or high-quality Ohmic contact. For example, Tongay *et al*. have used Br intercalation to tune the work function of multilayer graphene in connection with semiconductors, and consequently modified the barrier height and device performance of the Schottky diodes. Tang *et al*. have reported a uniform method for solution-processed doped films that are able to reach ultrahigh or ultralow work functions, which is essential for good Ohmic contact in device engineering [113,146,149–153].

The work function is also a critical property in electronic devices comprising multiple junctions, such as transistors. One case is the metal-oxide-semiconductor field-effect transistor (MOSFET) devices that are widely used in the micro- and nanoelectronics industry. The heart of a MOSFET is a metal-insulator-semiconductor (MIS) structure, in which the flat-band voltage, which is the gate voltage required to flatten the band bending in the near-interface region of the semiconductor base, is directly influenced by the work-function difference between the metal gate electrode and semiconductor base [146]. The flat-band voltage plays a significant role in determining the threshold voltage of a MOSFET, which is the most helpful parameter of the transistor [154]. Therefore, tuning work function of the gate metal (or base semiconductor) of the MOSFET could effectively tune the device performance. Examples of such tuning include using binary alloy systems [155] or *p*-doped gates on *n*-MOSFET devices [156] to control the threshold voltages. Additionally, as modern electronic devices are fabricated to be ever smaller, several effects induced by small length scales that cause drawbacks in device performance have become more significant. It has been suggested that these effects could be eliminated with proper work-function engineering. For example, Deb *et al*. has shown that a continuous work-function variation, created by alloy mole fraction variation in the gate electrode material, could suppress the drain-induced barrier lowering effect in silicon-on-insulator MOSFET devices [157]. Hou *et al*. demonstrated that an increase of gate electrode work function reduced the gate-to-channel tunneling in off-biased *n*-FETs, and the use of a metal gate with a midgap work function resulted in a significant reduction of gate to source and drain extension tunneling in both *n*- and *p*-FETs [158]. In multigate devices, work-function engineering is also relevant for more optimal device design. Researchers have suggested for the fin-FETs, the work-function variation on gates could affect the device performance parameters, such as threshold voltage [159] and current flow shape [160]. Proper electrode treatment for effective work-function engineering has been employed to improve fin-FET device performance [161].

Overall, for solid-state electronic devices, engineering the work functions of various materials comprising the heterostructures of a device is particularly critical for reaching desirable electrical connection and controlling device performance by tuning barrier heights. To sum up, the work function strongly influences the relative energy-level alignment across interfaces in solid-state electronic devices, therefore is one of the key properties to understand and to tune, in order to boost the device performance.

C. Catalysis

A chemical reaction is often accelerated by a solid catalyst that binds species relevant to the overall reaction. Such binding often involves electron transfer between the catalysts and the adsorbed reactants, typically involving the Fermi level of the catalysts and the highest occupied molecular orbitals (HOMOs) or lowest unoccupied molecular orbitals (LUMOs) of the reactants. Therefore, the catalytic behavior can correlate with the relative alignment between the catalyst Fermi level and the reactant orbital levels, and therefore with the work function of the catalyst. However, determining the expected qualitative relationship between work function and charge transfer between the catalyst and reactants needs careful consideration of contributing factors, as we illustrate below.

First, consider the case of a reactant or product that is essential to the rate-limiting step (RLS) of a reaction and is adsorbed on the surface of a catalyst in a way that includes some charge transfer (i.e., chemisorption). For simplicity, assume that approximately one electron is transferred from the catalyst to the adsorbate (e.g., F on Cu), the catalyst has a simple homogeneous surface, the

adsorbate has a fixed energy level to take the electron that is not altered by adsorption, and there are no external fields. All of these constraints can be easily relaxed without changing the qualitative trends implied by the following arguments, but the ideas are clearer for this simplified case. One might expect that the energetics of the electron transfer are related to the work function. To understand how this relationship emerges, think of the electron transfer as taking place in two steps: (i) the electron is removed from the clean catalyst surface to a local point, and then (ii) the electron is returned to the surface to reside on the adsorbate. The first step, by definition [see Eq. (3)], results in an energy cost equal to the local work function Φ. The second step results in an energy gain associated with moving the electron from the local point to the adsorbate. If the electron and adsorbate were both in the vacuum region, this energy would be, by definition, the adsorbate electron affinity (EA) (if the adsorbing species is giving out electrons, this will be the ionization energy IE). However, since the adsorbate is not strictly in vacuum in step (ii), there may be significant energy modification, which is denoted as an energy gain of ΔE. Thus, the energy of the charge-transfer process can be written as $\Phi - \mathrm{EA} - \Delta E$ per electron, or $n(\Phi - \mathrm{EA} - \Delta E)$ for n electrons, where n is positive for electrons transferred from the catalyst to the adsorbate. For a given adsorbate reactant and a series of catalysts, if we assume that the ΔE term (and the EA term, by definition) is approximately constant, then the energy to transfer electrons scales with the catalyst work function plus a constant shift. We propose that it is a reasonable qualitative assumption that the Gibbs free energy G_X of the binding of a species X consists of dominant chemical binding term that is proportional to the charge-transfer energy and a more modest charge-transfer-independent constant, G_X^0, i.e.,

$$G_X = \lambda n(\Phi - (\mathrm{EA} + \Delta E)). \tag{13}$$

Here λ is a reaction-specific coefficient of proportionality assumed to be positive (i.e., more energy gained in charge transfer will lead to a more negative binding energy that stabilizes binding). The $(\mathrm{EA} + \Delta E)$ and G_X^0 terms are expected to vary only modestly among catalysts with similar properties (which are considered as belonging to the same catalyst family), e.g., among all simple metals or all transition metal binary oxides.

This simple analysis suggests that for a given reactant, the binding energies associated with significant charge transfer should have a strong correlation with the catalyst work function for catalysts in the same family. However, such correlations are not expected to be exact, as many factors above we approximate to be constant may change to some extent between different catalysts (e.g., surface dipoles induced by the adsorbate, the adsorbate electron affinity or ionization energy, etc.), and the binding energy may not be exactly a linear function of the charge transfer. Since the adsorption energies of species in the RLSs largely control catalytic rates, we conclude that work functions and catalytic rates are likely to show correlation for a given reaction within a catalyst family.

Consistent with the preceding arguments and binding energy model, correlation between work function and catalytic rates is in fact well documented, as discussed below. Meanwhile, before we give examples, it is useful to consider extending the arguments just provided to electrocatalysts.

In many electrochemical reactions it is a good approximation to assume that the overpotentials are set by the relative Gibbs free energies of the adsorbates in the initial and final states of the RLS [162]. This can be written as

$$\eta = \frac{\Delta G}{ne} - E^0 = \frac{G_P - G_R}{ne} - E^0, \tag{14.1}$$

where η is the overpotential, G_X is the Gibbs free energy of the adsorbate state X, with P and R standing for product and reactant, respectively, n is the number of electrons transferred in the RLS, and E^0 is the standard potential for the reaction. Assuming binding energies behave as described above for the chemical catalysis case, then we expect that

$$\Delta G = G_P - G_R = \lambda(n_P - n_R)\Phi + C, \tag{14.2}$$

where λ is the proportionality coefficient, and C represents the contributions from $(\mathrm{EA} + \Delta E)$ and G_X^0 terms, as well as any other species within the P and R states that are not bound to the catalyst, e.g., ions formed in solution. Since the $(\mathrm{EA} + \Delta E)$ and G_X^0 terms likely do not vary much within the same catalyst family, and the contributions from the unbound species are independent of the catalysts, it is plausible that C is approximately constant within a specific catalyst family. Therefore, an approximately linear dependence of the overpotential on the work function of the catalyst is expected. It should be noted that the second term C in Eq. (14.2) is not expected to be small, and even modest variations between catalysts could wash out the work-function dependence of the first term in Eq. (14.2). It is therefore likely that Eq. (14.2) is only applicable in limited situations, and particularly for cases where the catalyst family has very strong similarities (e.g., as might occur for a series of Pt-group metal catalysts).

As a concrete example, for water splitting in acid, the adsorbed intermediates have been proposed to be, in order of their formation, O_2*, $HOO*$, $O*$, and $HO*$, where * denotes a surface adsorption site [162]. If the $HOO* \rightarrow O*$ reaction were the RLS, then the overpotential would be set by the Gibbs free energy of reaction for $HOO* + e^- \rightarrow O* + OH^-$, which we denote as $\Delta G_{O^*-HOO^*}$. For fixed applied potential, pH, and temperature, the only terms that change with catalysts are the

energies of the species on the surfaces, i.e., $\Delta G_{O^*-HOO^*} = G_{O^*} - G_{HOO^*} + C' \approx \lambda(n_{O^*} - n_{HOO^*})\Phi + C$. Here we use the expression for binding energy from Eq. (13) and C' and C are terms assumed to be approximately constant within a catalyst family. Given the different oxygen content of O∗ and HOO∗, it is likely that $n_{O^*}$and n_{HOO^*} are quite different, leading to a strong dependence of $\Delta G_{O^*-HOO^*}$ on the catalyst work function. The correct RLS for water splitting in acid on metal catalysts is generally believed to be the reaction $OH* + H^+ + e^- \rightarrow H_2O\,(\text{liquid}) + *$ [162]. If we assume this is correct, then, following the same argument given for the previously discussed RLS step, it could be predicted that the overpotential for water splitting is approximately $\Delta G_{OH^*-*} \approx \lambda(n_{OH^*})\Phi + C$, where C represents a term approximately constant across similar catalysts.

We now describe some computational and experimental examples demonstrating the correlations implied by the preceding binding energy model [Eq. (13)] and associated arguments. We note that Eq. (13) implies that the binding energy trend with Φ has a slope that depends on the sign of the charge transfer. We define two types of (electro)chemical reactions: "electrophilic" [reductive for the adsorbate(s)] reactions are ones where the RLS benefits from binding species that effectively take electrons from the catalyst and place them on the adsorbate(s). In contrast, "electrophobic" [oxidative for the adsorbate(s)] reactions are ones where the RLS benefits from binding species that effectively take electrons from the adsorbate(s) and place them on the catalyst. We would expect that electrophilic (electrophobic) reactions have negative (positive) trends in relevant binding energies and associated reaction rates with catalyst work function.

An example of such trends in experiments are given by the empirical observation from by Vayenas *et al*. that for non-Faradaic electrochemical modification of catalytic activity (NEMCA) [163,164], the catalytic reaction rate r exponentially depends on the catalyst work function Φ through

$$\ln \frac{r}{r_0} = \alpha \frac{\Phi - \Phi^*}{kT}, \tag{15}$$

where α and Φ^* are reaction- and material-specific constants. Vayenas *et al*. found that α is positive (negative) for an electrophobic (electrophilic) reaction, just as is implied by our analysis above. Furthermore, our arguments suggest that activation energies for RLS, which tend to correlate to binding energies, will be linear in the catalyst work function. Thus, the linear dependence of $\ln(r)$ on work function is very consistent with our model. Linear dependence of $\ln(r)$ on work function is quite common throughout the examples below.

Further supporting our model is that a generally negative dependence between the catalyst work function and catalytic reaction rate has been frequently observed for many "electrophilic" reactions. For example, Cheon *et al*. found a linear decrease in electrochemical oxygen reduction reaction (ORR) current density as the work function of a doped nanocarbon catalyst increases [114]. Stoerzinger *et al*. and Hong *et al*. have studied $LaMnO_3$-type perovskites, and showed that the work function correlates to the ORR rates by indicating the interfacial band bending related to electron transfer during such reactions [165,166]. The work from Trasati [167], Calle-Vallejo *et al*. [168], and Losiewicz *et al*. [169] on hydrogen evolution reaction (HER) all show that the HER exchange current increases exponentially as electrode work function decreases, where the negative correlation is consistent with the reaction being fundamentally reductive.

Similarly, abundant examples also indicate the opposite (but expected) trend for "electrophobic" oxidation reactions. Kumar *et al*. showed that the methane oxidation activation energy decreases linearly (i.e., reaction rate increases exponentially) with the increase of a series of catalyst work functions [170], consistent with the reaction being oxidative. Similarly, as reported by Vayenas *et al*., the NEMCA in oxidation reactions with β"-Al_2O_3 is exponentially increasing with the catalyst average work function. Grimaud et al. demonstrated the oxygen evolution reaction (OER) current density of perovskite catalysts positively correlates with the oxygen p band [171–174], which in turn correlates positively with work function [10,100].

A somewhat counterintuitive example of catalyst trends with work function is that a number of studies have shown the oxygen surface exchange coefficient in perovskites, k^*, also correlates positively with the oxygen p band [171–173] and therefore positively with work function. For all of the systems studied in deriving these positive correlations the mediating species for the oxygen exchange process that set k^* are oxygen vacancies, which reduce the catalyst when they are formed and are therefore "electrophobic" reactions. Thus, the positive correlation between k^* and work function is consistent with the trends expected from our above analysis and Eq. (13). Interestingly, Lee *et al*. [175] showed that for a set of interstitial oxygen transport materials k^* was negatively correlated with work function. For these materials, the mediating species for the oxygen exchange process that set k^* are oxygen interstitials, which oxidize the catalyst when they are formed and therefore represent an "electrophillic" reaction. Thus, the negative correlation between k^* and work function in these materials is also consistent with the trends expected from Eq. (13). In summary, all the above correlations between catalyst or electrode work functions and reaction characteristics are consistent with the qualitative and in some cases even quantitative implications our above analysis based on Eq. (13).

In general, we expect significant correlation between work function and the energetics of any process involving

exchange of electrons at the material surface, such as surface adsorption, charge transfer, and redox. Thus, it is possible to tune catalytic properties of specific electrochemical reactions by tuning the work function of the catalyst surface [36,176]. These results, and many others, suggest work-function engineering is a critical tool when designing high-performing catalysts.

D. Work function for materials design with targeted mechanical properties

Qualitatively, the work function is a measure of how strongly a material binds electrons. As electron binding strength is deeply intertwined with overall chemical bond strength, it is reasonable to expect there are relationships between work function and mechanical properties of materials. Hua and Li showed there is a simple relationship between Young's modulus E of polycrystalline elemental metals and their corresponding (polycrystalline) work function, $E = \alpha\phi^6$, where α is about 0.02 GPa/eV^6 [177]. It is worth noting that there is some significant spread in the data, and a range of 0.5 to 2 times this quoted α value of 0.02 is needed to fully bound the dynamic range of the data [178]. This sixth-power scaling law of Young's modulus to work function can be modified to also correlate yield strength and hardness with work function, provided the Poisson ratio of the material is known [179]. Lu and Li also extended their previous work to include correlations of work function with bulk modulus, thermal expansion coefficient, and Debye temperature [180]. We note here the quality of fits for yield strength and hardness do not seem as robust as that of Young's modulus, likely reflecting the fact that yield strength and (particularly) hardness are sensitive to the material microstructure and associated dislocation dynamics responsible for deformation, and are thus not strictly intrinsic materials properties. In addition, the relationships described above all involve polycrystalline, elemental metals, and the performance of these scaling laws to include alloys and more complex microstructures (e.g., those with mixed phases) appears to be largely an open question.

Some correlations between work function and mechanical properties in alloys has been demonstrated. For example, Lu *et al*. [181] correlated the change in Young's modulus and hardness of X70 steel alloys with varying amounts of Ni with the corresponding change in work function as measured using a scanning Kelvin probe. Given the higher work function of Ni compared to Fe (the primary component in X70 steel), it was observed that increasing the Ni content led to an increase in work function and a corresponding increase in the measured Young's modulus. Once greater than 10% Ni was added, and particularly once at least 30% Ni is added, the material shows phase separation between the original X70 phase and a Ni-rich $FeNi_3$ secondary phase. This secondary phase was shown to have lower hardness and lower measured work function than the parent X70 material. This result is interesting as it demonstrates that microstructural patches of X70 and $FeNi_3$ phases display patchy work-function behavior *and* different local hardnesses. A follow-on study by Li *et al*. further connected work-function differences and their associated potential drops across material interfaces with the mechanical quality of the formed interface [182].

Overall, the work function of metals is physically connected to the underlying bond strength, thus forming a link between work function and the mechanical and thermal properties of materials. Work in this space has focused primarily on polycrystalline elemental metals, but the study from Lu *et al*. on X70 steel indicates that correlative relationships persist when considering metal alloys as well. Additional work in this space to make and validate empirical relationships between work function and mechanical properties of alloys and complex microstructures with a distribution of different material phases could be helpful for guiding the design of materials with targeted mechanical properties.

E. Other applications: energy harvesting, water splitting, solid-state batteries, gas sensing

Work-function-based energy-level alignment serves as a useful guide for a number of related applications.

Work function has been involved as a key factor in many energy-harvesting applications, i.e., transforming other forms of energy to electricity. Thermal energy can be harvested directly from thermionic emission through so-called thermionic converters, in which alkaline metal adsorption from the vapor is the primary approach to lower the cathode work function [42,183]. In solar photovoltaics used to harvest photon energy, similar to solid-state electronics, work function serves as a factor for controlling charge transfer. For example, as pointed out by Qi and Wang [184], when the electrode-active layer contact in the organic solar cell is non-Ohmic, the open-circuit voltage will largely depend on the work-function difference of the electrodes. It has also been suggested that the built-in electric field, open-circuit voltage, and efficiency of Si-based and organic photovoltaic cells strongly correlates with work functions of the transparent conductive oxides (TCO), and a higher work function is generally preferred [115,185–187]. Recently, tuning the band alignment (thus work function) of the electron and hole transport layer materials has been one of the key factors contributing to the recent boost of the halide perovskite [e.g., using methylammonium lead iodide ($MAPbI_3$)] solar-cell efficiency to nearly 25% [102,188,189]. Additionally, Varpula *et al*. reported an approach to harvest mechanical energy from two electrodes with different work functions by vibrating one electrode relative to the other [190]. Because the work function difference between electrodes introduces a

built-in electric field, such electrode motion will do work in the field, transforming kinetic energy of the electrode to electrostatic energy.

In a photocatalytic water-splitting reaction, the water molecules decompose into H^+ ions and O_2 after absorbing photons and holes, and H^+ ions combine with electrons to form H_2. Thus, a key process is separating electrons and holes before recombination, in which case proper band alignment plays a significant role. Beasley *et al*. have studied a series of metals in the metal-TiO_2 heterostructure for photocatalytic water splitting and discovered a linear increase of hydrogen production with the increase of metal work function in the heterostructure [191]. This is because a higher metal work function makes it energetically more difficult for electrons to transfer back to TiO_2 to initiate electron-hole recombination, resulting in a higher hydrogen yield. Similarly, for water-splitting photoelectrochemical cells, Ye *et al*. have also tuned the C_3N_4 electrode work function by boron doping to enhance the charge separation [192]. Meanwhile, they have also managed to reduce the interfacial energy loss and increase the open-circuit voltage of $BiVO_4$ photoelectrochemical cells by tuning the work function via Mo doping, which is also beneficial for water splitting.

Band alignment is also involved in many studies on batteries. Recently, Gao *et al*. [193] have studied the gassing issue of the spinel $Li_4Ti_5O_{12}$ anode of the lithium-ion battery, pointing out that the Li-rich surface and oxygen vacancies lower the anode work function, which translates into an increasing chemical potential that greatly promotes the interfacial reaction of electrolyte decomposition. Warburton *et al*. have investigated the interfacial thermochemistry and band alignment of a solid-state Li-ion battery with lithium lanthanum titanate electrolyte (LLTO) using DFT calculations [194]. The study points out the TiO_2-terminated surface is more likely to be involved in redox reactions because the conduction-band minimum of LLTO is lower than the Fermi level of metallic Li anode, when aligning the vacuum level together, which makes electron transfer to LLTO more favorable, leading to the decomposition of the electrolyte by reducing Ti^{4+} cations to more reducing states. This could explain the tendency for decomposition of TiO_2 terminated LLTO. Such band alignment also shows the difficulty of charge transfer in the presence of a La_2O_3 buffer layer, suggesting its potential application as an interface coating material.

There are also numerous examples related to other application aspects. For example, Li *et al*. have investigated using TiO_2-SnO_2 core-shell heterostructure nanofibers for gas sensing [195]. In such a heterostructure, TiO_2 has a lower work function (4.2 eV) compared to SnO_2 (4.9 eV), meaning that extra electrons will flow from TiO_2 to SnO_2, significantly increasing the detection response towards acetone and ammonium.

V. MECHANISMS OF WORK-FUNCTION ENGINEERING

Since work function depends on the bulk electronic structure and surface dipole, there exist two main strategies to realize work-function engineering. They are (1) tuning the bulk electronic structure, i.e., setting the location of the Fermi level, or (2) tuning the surface dipole to modify the surface potential. It should be noted that many work-function engineering approaches, such as doping and composition tuning may vary these two factors simultaneously, in which case the work-function change is a mixed effect [10,85,187].

A. Tuning the Fermi level

Assuming a rigid band model, the Fermi level can be directly modified by doping free carriers into the material. On the other hand, it is also possible to alter the shape of the band structure by composition changes, oxidation state variation, and defects.

The first approach we discuss is to dope the bulk material. The dopant atoms will not only provide excess free carriers, but also add dopant energy levels that modify the original band structure, and both of these effects will change the electron filling level [187,196]. This doping strategy is typically employed in semiconductors or transition metal oxides. Klein *et al*. have studied transparent conductive oxides (TCOs) such as Al-doped ZnO, SnO_2, and ITO [187], and quantified the Fermi-level shift and work-function change in terms of dopant and material processing methods. As shown in Fig. 11(a), the work function is negatively related to the Fermi level. That is, the work function decreases as the Fermi level is increased above the VBM. As mentioned in Sec. I B, it is hard to derive a clean linear relationship between these two quantities because it is not possible to fully decouple the surface-dipole effect when taking the Fermi-level shift into account.

In the limit of very high doping levels (e.g., a few percent or more), the material is effectively alloyed, and the composition is tuned significantly, leading to significant changes to the band structure. This is typically the case of work-function engineering via Fermi-level modification in transition metal oxides, in which case not only the electron filling level has been changed, but also the band structure. It could be imagined that with high composition flexibility, composition tuning can be used for more precisely altering the band structure. Meanwhile, the electronic band structure might also vary with the cation chemical states or defect concentrations, especially for transition metal oxides, in which the cations may adopt different *d*-band filling levels associated with stoichiometry and oxygen vacancy concentration. Greiner *et al*. measured the work function for a set of transition metal oxides [198]. Their work suggests that the work function decreases with

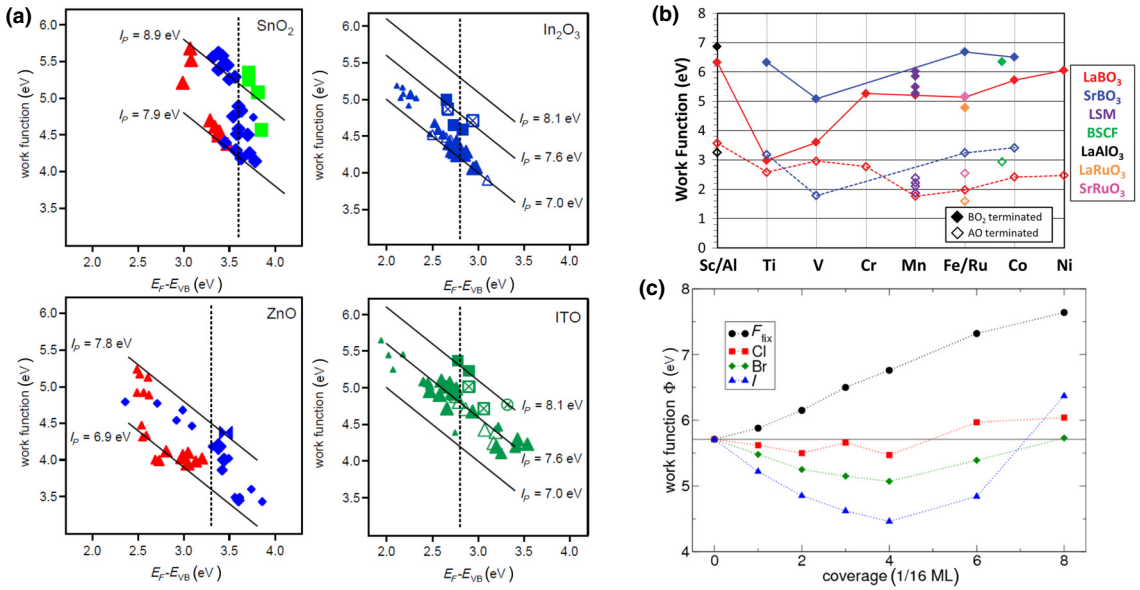

FIG. 11. Different work-function tuning mechanisms. (a) The work-function dependence of Fermi level for different TCOs (from Ref. [187]. Copyright: open access, credit to the original authors). (b) Computational results for a series of perovskite (001) work functions with different terminations (typically AO and BO_2 terminations have opposite dipole moments) (from Ref. [10] ©2016 WILEY-VCH Verlag GmbH & Co. KGaA, Weinheim). (c) DFT-calculated platinum electrode's work function dependence on different adsorbed halide functional groups (from Ref. [197]. Copyright: open access, credit to the original authors).

decreasing cation oxidation states and increasing oxygen vacancy concentration [198], which could be attributed to increasing donor doping states associated with oxygen defects, and higher concentration of low electronegativity cations.

Another possible way to tune the bulk electronic structure is to introduce strain into the original material. Peng *et al*. have studied the work function of armchair graphene nanoribbons (AGNRs) under different strain states with DFT calculations [199], and saw an increase in work function under tensile strain. This change could mainly be attributed to the changes in Fermi level associated with bulk electronic structures evolution under different strain states, since the local vacuum level barely changes during this evolution.

The work-function modification magnitudes realized from doping, significant composition changes, and strain, are varied. By altering the material composition and cation-valence states, the work function could change by a few tenths of an eV to up to a few eV when the band-filling levels become significantly altered. Strain, in contrast, generally has a minor effect on the band structure compared to the changes resulting from compositional and valence-state effects, making the modification of work function smaller, typically on the order of 0.1 eV [10,85,198,199].

Another example of tuning the Fermi level of the material is represented by *negative electron affinity* materials. In these materials, the Fermi level is tuned to be in the conduction band, and the vacuum level lies within the band gap, below the conduction-band minimum. Materials with such properties, with the most widely known example being diamond with adsorbed H, are promising candidates for field emitters and photocathodes, provided the surface features necessary to have negative electron affinity can be maintained during emission [124,125,200].

B. Tuning the surface dipole

In addition to tuning the bulk electronic structure, an alternative approach is to modify the surface dipole. Some studies have argued there are two distinct mechanisms related to surface-dipole modulation, namely adsorbate-induced dipole and charge transfer-tuned dipole [199]. Sometimes there will be charge transfer between the bare solid surface and adsorbates during adsorption, making the total dipole moment a mixed effect of altering the surface dipole and modifying the electronic structure and Fermi level in the near-surface region of the material.

The scale of surface-dipole effects can be understood in terms of the Helmholtz equation, which gives the relationship between work-function change $\Delta\Phi$ and surface-dipole density from an electrostatic potential perspective:

$$\Delta\Phi = -\frac{e}{\varepsilon_0}\mu_z(N)N. \tag{16}$$

Here, e is the elemental charge, N is the density of surface molecules, and $\mu_z(N)$ is the dipole moment per molecule that is perpendicular to the surface [78,201]. This equation can be understood by considering the surface dipole as a charged parallel capacitor, and the resulting work-function

change equals the potential energy change when an electron passes through the capacitor. Such a model is well supported by numerous computational works, showing that after applying reasonable estimates of dipole density and moments, the Helmholtz equation gives good estimations for the work-function modifications [163,202,203].

Every solid surface has its own intrinsic dipole, originating from broken symmetries and dangling bounds on the surface [11]. With further surface treatments, such as adsorption of functional groups or sputter etching, this dipole can be modified in a purposeful way. For example, the adsorption of Cs or Ba species will lower the work function of W dispenser cathodes [112], and hydrogen plasma dry etching has been observed to enhance field-emission performance of silicon nanowires [204].

1. Exploring materials with intrinsic dipoles

Typically, intrinsic surface dipoles have small magnitudes, especially for metals and metal alloys, and therefore a small effect on work function (typically on the order of a few tenths of an eV). As discussed in Sec. I B, conduction electrons in metals and alloys are well modeled as an ideal Fermi gas, and their surface dipoles are mainly from smoothing or spreading, where the actual elemental composition near the surface and associated charge plays a small role [9]. Thus, the work functions of most metals are 4 to 5 eV, except for alkali and alkaline earth metals, which generally have work functions around 2 to 3 eV. Furthermore, the work-function differences between different orientations and surface terminations for metal systems are small, around 0.3 to 0.5 eV [91,205].

However, in more chemically complex material systems, such as oxides, the simple Fermi gas model is no longer applicable since the electrons are mostly ionically or covalently bonded or localized near the ions. The distinct charge states among different elements cause large variations in both the Fermi and vacuum levels for different materials and different surface terminations, resulting in a large spread of work functions from approximately 0.85 eV for Cs_2O [206] to 7 eV for V_2O_5 [207]. This 7-eV value for V_2O_5 is much higher than the work function of refractory metals like Mo and W, partially because of the large surface dipole of V_2O_5. For chemically complex materials like oxides, due to the electronegativity differences among different compositional elements, the topmost atomic layer and the layer beneath may lie in different charge states, forming a polar surface with a large dipole moment, where the dipole moment could result in an effect of a few eV in magnitude if estimated by the Helmholtz equation. In these cases, tuning the intrinsic dipole moment may be an appealing approach for work-function engineering [10,14,85,86,208]. In first-principles calculation works by Jacobs *et al*. [10] and Zhong and Hansmann [85], the (001) AO-terminated and BO_2-terminated work functions in perovskite ABO_3 compounds are predicted to differ by over 4 eV. For example, according to Jacobs *et al*., SrO-terminated $SrVO_3$ is predicted to have a 1.86 eV work function, whereas the VO_2-terminated counterpart is predicted to be 5.89 eV. This large work-function range of oxides is also evident from experiments. Chambers *et al*. measured the work functions of (001) SrO- and TiO_2-terminated Nb-doped $SrTiO_3$ [86], showing a 1.5-eV difference between these two terminations. Similarly, the origin of low work function surfaces in some commercial thermionic emitter materials such as LaB_6 and CeB_6, can also be at least partially attributed to an intrinsic dipole moment between the cation layer and boron framework [141,142]. These studies suggest that by exploring material systems, tuning compositions, and selecting surface orientations and terminations, it may be possible to access a wide range of work-function values by altering surface dipole moments. Although recent studies have focused on perovskites, other material systems, which can stabilize the intrinsic polar surface would be of interest for using this polarity to engineer work functions.

To achieve stabilization of intrinsically highly polar surfaces it is likely that materials with high electrical conductivity (for example, conductive oxides) are needed. Typically, strongly polar surfaces are not stable due to the additional electrostatic energy introduced by the strong surface dipole [209]. Insulators compensate such a dipole with surface adsorption or reconstruction, diminishing the intrinsic dipole moment [95,210]. On the other hand, with enough free electrons, metallic systems can simply screen such a dipole moment by moving electrons [80,211]. In order to achieve metallic behavior in oxides, transition-metal elements should be included to provide additional electrons for the formation of a partially filled conduction band. This explains why, as mentioned above, perovskites have been investigated for work-function engineering with an intrinsic dipole moment. Other conductive oxides, such as spinels [212] or Ruddlesden-Popper phases might also be amenable to significant, stable intrinsic surface dipoles. We suggest that it is an open research opportunity to further explore these and related materials systems for promising work-function-engineering material candidates.

2. Additional surface treatment to modify the dipole

Although the surface dipoles could be in principle tuned by exploring compositions and structures of different materials, in practice it is often challenging to find a material that has both a significant surface dipole and good properties in other application aspects, such as melting point, electrical conductivity, mechanical strength. Therefore, modifying the surface dipole by surface treatments of the base material for the proposed application may offer more practical appeal. Several examples of such

treatments include introducing surface adsorbates, adding buffer layers, and etching the original surface.

A good example of this surface treatment approach is the dispenser cathode, which is mentioned in the above sections. During operation, the high temperature of the cathode vaporizes the Ba in the impregnates and enables a BaO monolayer to form on top of the tungsten body, creating a large surface dipole that reduces the W intrinsic work function by over 2.5 eV [112,201].

Besides the case of BaO-impregnated dispenser cathodes, GaAs and $Al_xGa_{1-x}As$ photoemitter work functions are modified by cesiation of their surfaces. Additionally, other functional groups, such as halides, -OH or -H, -O (or O_2), have also been used for modifying the work function of graphene, MXene, bare metals, etc. [197,199,213–216]. The work-function modification is typically associated with charge transfer between the base material and the functional group. Generally, the surface species with higher electronegativity, such as -O, tends to attract electrons from the material, creating a dipole that increases the work function. Other adsorbates such as -H tend to donate electrons and create dipoles that decrease the work function [199]. However, according to Leung *et al*. [215], this is not always the case as the charge transfer and the electron-cloud behavior could be complex on the surface. In some cases, for example O on W, the work function may decrease for certain arrangements of O on W when the spreading of the electron-cloud tail creates a positive effective dipole relative to its clean surface counterpart.

Surface dipoles are also modified by other surface-treatment methods, such as sputtering and chemical etching [217–219], which are effective approaches for work-function engineering for specific applications. For example, Joo *et al*. explored BCl_3/Ar plasma etching of Al-doped ZnO thin films, reporting a 200 meV work function increase resulting from this treatment [218]. Bruening *et al*. studied the effect of chemical etching of CdSe, reporting significant modifications of the work function, including increases of 0.5 to 0.7 eV with oxidizing etching, and decreases of 0.3 eV with a following reducing etching [219].

VI. SUMMARY AND OUTLOOK

In this paper, we review the basic physics of work function, its measurement and prediction methods, followed by applications and mechanisms of work-function engineering. We review the fundamental physics regarding the work-function definition, especially the role of patch and applied fields, clarifying the local nature of surface intrinsic work function and introducing the concept of the observed work function. We review the physics determining the work function, emphasizing the roles of bulk electronic structure and surface dipole. We review the common work-function measurement methods together with their advantages and limitations. For the canonical photoemission-based method, we summarize and stress some finer points related to correctly performing and interpreting results of photoemission experiments and discuss the influence of patch-field effects on work-function interpretation. For common methods of extracting work-function values from electron emission, we emphasize the relevance of citing both the fitted work function and prefactor constants. We review the DFT prediction method and the recent development of machine-learning approaches, showing their power in work-function calculation and understanding. We summarize some particularly useful fields among the vast applications of work-function engineering. We point out the two main strategies of work-function engineering based on work-function physics, namely tuning bulk electronic structures and surface dipoles.

Given the significance of work-function engineering, and the existing unsolved problems of its fundamental physics, there are many current and future research opportunities. We discuss some of these future opportunities below.

A. Work-function and electron-emission physics and models

In this review, we discuss the work-function behavior under different field conditions, especially under the patch field induced by surface heterogeneity. However, this understanding is still only in the nascent stages. For example, the discussion in this review focused only on a simplified flat surface with two kinds of patches that differ only in local work functions (i.e., with identical sizes and shapes). On real surfaces, the physics is generally more complex. For example, the surface can have more than two local work-function components, with different patch sizes and shapes. Many emitting cathode surfaces will be porous and rough, rather than smooth. The roughness may affect emission through local electric field enhancement, porosity may result in electron emission from within pores, and complex realistic morphology will generally result in complex space-charge electric fields. Quantitative theoretical predictive models incorporating these effects are needed to accurately predict critical characteristic parameters of photo, thermionic, and field electron emission, such as onset photon energy, current density versus temperature and applied voltage, spatial distribution of emission current, discrepancy between fitted and theoretical Richardson constant values, beam shape, and emittance.

The discussion on fundamental work-function physics in this review has mainly focused on metals. Given the technological significance of semiconductors in micro- and nanoelectronics, fuel cells and solar cells, electrocatalysis and water splitting, it is useful to understand how ionization energy, electron affinity, and work function behave

under different field conditions, with few mobile carriers, wide interfacial charge regions, and energy band bending on the surfaces and interfaces.

B. Computational work-function predictions

In the past few decades, considerable progress has been made on predicting work function with computational tools. However, exciting and further opportunities remain.

First, there are still relatively large disagreements between computationally predicted and experimentally measured work-function values, especially for complex materials and surfaces. This can be partially attributed to the difficulty in capturing the exact surface structures for these systems, which, in turn, affects other surface electronic and chemical properties. Therefore, advanced models are needed to more accurately predict work functions and many related surface phenomena on complex surfaces. Additionally, leveraging machine-learning approaches for work-function prediction is still at the nascent stage. Present models still have relatively large prediction errors and limited domains of applicability. This leaves great opportunities for future research, to expedite work-function predictions on complex material systems and reveal nuanced physical relationships between work function and other material and surface properties.

C. Work-function engineering targeting various application needs

Across different application areas, there is an increasing demand for optimizing device performance by tuning the work function of a material to realize desirable band alignments and other properties.

For example, low work-function materials with high electrical conductivity, robust stability, and good mechanical properties would make promising candidates for next-generation electron emitters. Recent research results show the potential benefits of discovering how to weaken patch electric fields by reducing local work-function heterogeneity and enlarging emission surface patch sizes.

In solid-state electronics, properly tuning the electrode work function with advanced specific materials would enable further optimization of the electron migration behavior across interfaces. This has potential for advanced device applications such as designing high-frequency Schottky diodes with proper barrier height, or controlling threshold energy and suppressing small-size drawbacks for MOSFETs. Moreover, it will enable deeper understanding of how the electrode work function couples with other interfacial phenomena, such as interfacial states and oxide charges, to influence the device performance.

Carefully controlling the energy-level alignment between catalysts (i.e., the work function, ionization energy or electron affinity) and reactant species (i.e., HOMO or LUMO), should significantly improve the performance of a material in catalytic reactions. There are also opportunities to enhance the charge separation in water splitting and suppress the interfacial degradation in solid-state batteries with proper work-function engineering.

D. *In situ* work-function measurement, and connection between work function and exact surface structure

Accurate measurement of work function is a crucial research topic in surface science. As discussed in Sec. II, various methods have been employed to measure the work function. However, these methods are generally conducted *ex situ* and are therefore unable to characterize the surface structures and chemistry under the application conditions. Since the work function is extremely sensitive to the surface changes, these *ex situ* measurements may yield misleading discrepancies between the measured work functions and their actual values under the application conditions. Advanced characterization methods that could measure the work function *in situ* and thus connect the work function with the surface microstructures and behaviors during device fabrication and operation, would enable deeper fundamental materials science insights and device performance optimization.

Given the significant impact of patch fields on emission energy barriers and observed work functions, it is critical to properly configure experiments (e.g., applied electric field and probing distance) for correct local work-function measurements. Furthermore, advanced *in situ* measurements of work-function distributions on heterogeneous surfaces would provide valuable insights on the influence of local work-function heterogeneity in various applications.

E. Systematic investigations of materials for work-function engineering

It has been proposed that several material systems are naturally suitable for work-function engineering because of the high tunability of their electronic properties (i.e., bulk Fermi-level position and surface dipole). Therefore, another opportunity involves systematic investigation of bulk materials or surface species that are suitable for work-function engineering, including polar oxides such as perovskites and spinels, or different functional groups (fluorine, hydroxide, alkaline, or alkaline-earth metal species, etc.). Many of these materials with extreme work functions tend to be less stable, presenting research opportunities for fundamentally understanding and controlling their instabilities.

ACKNOWLEDGMENTS

This work is funded by Defense Advance Research Project Agency (DARPA) through the Innovative Vacuum Electronic Science and Technology (INVEST) project.

TABLE I. Quantities and values related to work-function physics.

Quantity	Equation	Value
Distance from cathode that image-charge potential is negligible (local distance)	$E_{\text{img}}(d) = -\dfrac{e^2}{16\pi\varepsilon_0 d}$	5 nm
Negligible energy for applications with work-function change (image-charge potential change from 5 nm to infinity)		0.07 eV
Typical upper bond of weak field (lowering the barrier by 0.07 eV)	$\Delta\Phi = \sqrt{\dfrac{e^3F}{4\pi\varepsilon_0}}$	$\sim 10^6$ V/m
Typical lower bond of strong field (lowering the barrier by 0.4 eV)		$\sim 10^8$ V/m
Critical field for 1-mm patches with 1-eV work-function difference	$F_0 = \dfrac{\Phi_H - \Phi_L}{ek\sqrt{S}}$	$\sim 10^3$ V/m
Critical field for 1-μm patches with 1-eV work-function difference		$\sim 10^6$ V/m

CONFLICT OF INTERESTS

The authors have no conflict of interests to declare.

APPENDIX I: VALUES OF CUTOFF ENERGY, DISTANCE, ELECTRIC FIELD, AND PATCH FIELD

In Sec. I we discuss many quantities related to work-function definitions and their behavior under different field conditions. This Appendix section describes our precise definitions for what we consider negligible, small, large, etc. This section provides a set of self-consistent values of these quantities that is valid for typical applications involving work function from the equations mentioned in Sec. I.

We first derive a distance where the image-charge potential energy is negligible based on Eq. (2), in which case the electron could be considered as no longer being influenced by the solid surface. Typically, a length of "several nm" is quoted by researchers as the distance that the electron is far enough from being impacted by the surface. At this range the magnitude of the image-charge potential energy (compared to 0 at infinity) is not larger than approximately 0.1 eV, which is negligible in most applications in which the work function is involved. To set a simple specific value for this work, we select this distance as 5 nm, corresponding to a −0.07-eV image-charge potential energy.

Next, we evaluate the relative strength of the (negative) applied electrical field to determine if we are in low or high (or neither) field limits relative to the image charge by considering the magnitude of the Schottky effect [Eq. (5)]. We define a weak field as one that leads to a negligible lowering of work function due to the Schottky effect. If we assume the same 0.07 eV as used above as a negligible energy is straightforward to show that the for Schottky barrier lowering is 0.07 eV for a field of 3×10^6 V/m (or approximately 10^6 V/m). Thus, any electric field less than this value will be considered as a weak field in this work. On the other hand, if the applied field could cause a barrier lowering much larger than this value, such lowering is then significant in many applications. We take 0.4 eV as a clearly significant lowering of the work function. If we solve for the field that leads to an 0.4 eV lowering from the Schottky effect [Eq. (5)] we get 1×10^8 V/m, and we consider any value equal or greater than this as a strong field. The fields between 10^6 and 10^8 V/m are intermediate and will have a modest effect whose significance has to be assessed based on the specific situation.

Another area where certain assumptions are needed is when we evaluate the interplay between the patch field and applied field, based on Eqs. (6.1) and (6.2) in the main text. In this case, the observed work function strongly depends on the applied negative field even if it is in the weak-field scenario discussed above. Here we just provide two examples, showing the critical field for macroscopic and microscopic patches. Assuming the local work-function difference between the lower and higher work function patches is 1 eV, and neglecting refactors on the order of magnitude of 1, the critical field for a surface with 1 mm (1 μm) patches is 10^3 V/m (10^6 V/m).

In Table I we summarize the above-discussed quantities, the associated equations, and the typical values. It is noted that by simply plugging different values in these equations, one can adjust these quantities for any conditions or constraints.

[1] C. Kittel and P. McEuen, *Introduction to Solid State Physics* (Wiley, New York, 1996), Vol. 8.
[2] A. Kahn, Fermi level, work function and vacuum level, Mater. Horiz. **3**, 7 (2016).
[3] D. Cahen and A. Kahn, Electron energetics at surfaces and interfaces: Concepts and experiments, Adv. Mater. **15**, 271 (2003).
[4] D. Chen, R. Jacobs, D. Morgan, and J. Booske, Impact of nonuniform thermionic emission on the transition behavior between temperature-and space-charge-limited emission, IEEE Trans. Electron Devices **68**, 3576 (2021).

[5] W. Schottky, Über kalte und warme elektronenentladungen, Z. Phys. **14**, 63 (1923).

[6] J. A. Becker, Thermionic electron emission and adsorption Part I. Thermionic emission, Rev. Mod. Phys. **7**, 95 (1935).

[7] J. Trigueiro, N. Bundaleski, A. G. Silva, and O. M. N. D. Teodoro, Influence of the patch field on work function study using the onset method, Vacuum **98**, 41 (2013).

[8] N. Bundaleski, J. Trigueiro, A. G. Silva, A. M. C. Moutinho, and O. M. N. D. Teodoro, Influence of the patch field on work function measurements based on the secondary electron emission, J. Appl. Phys. **113**, 183720 (2013).

[9] R. Smoluchowski, Anisotropy of the electronic work function of metals, Phys. Rev. **60**, 661 (1941).

[10] R. Jacobs, J. Booske, and D. Morgan, Understanding and controlling the work function of perovskite oxides using density functional theory, Adv. Funct. Mater. **26**, 5471 (2016).

[11] K. Oura, V. G. Lifshits, A. A. Saranin, A. V. Zotov, and M. Katayama, *Surface Science: An Introduction* (Springer Science & Business Media, New York, USA, 2003).

[12] W. Kohn and N. D. Lang, Theory of metal surfaces, Phys. Rev. B **3**, 1215 (1971).

[13] H. Ishii, K. Sugiyama, E. Ito, and K. Seki, Energy level alignment and interfacial electronic structures at organic/metal and organic/organic interfaces, Adv. Mater. **11**, 605 (1999).

[14] T. Ma, R. Jacobs, J. Booske, and D. Morgan, Understanding the interplay of surface structure and work function in oxides: a case study on $SrTiO_3$, APL Mater. **8**, 071110 (2020).

[15] L. W. Swanson and P. R. Davis, 1. Work function measurements, Methods Exp. Phys. **22**, 1 (1985).

[16] J. W. Kim and A. Kim, Absolute work function measurement by using photoelectron spectroscopy, Curr. Appl. Phys. **31**, 52 (2021).

[17] S. Hüfner, *Photoelectron Spectroscopy: Principles and Applications* (Springer Science & Business Media, New York, USA, 2003).

[18] Y. Park, V. Choong, Y. Gao, B. R. Hsieh, and C. W. Tang, Work function of indium tin oxide transparent conductor measured by photoelectron spectroscopy, Appl. Phys. Lett. **68**, 2699 (1996).

[19] T. Schultz, T. Lenz, N. Kotadiya, G. Heimel, G. Glasser, R. Berger, P. W. M. Blom, P. Amsalem, D. M. de Leeuw, and N. Koch, Reliable work function determination of multicomponent surfaces and interfaces: The role of electrostatic potentials in ultraviolet photoelectron spectroscopy, Adv. Mater. Interfaces **4**, 1 (2017).

[20] O. Renault, R. Brochier, A. Roule, P. H. Haumesser, B. Krömker, and D. Funnemann, Work-function imaging of oriented copper grains by photoemission, Surf. Interface Anal. **38**, 375 (2006).

[21] M. G. Helander, M. T. Greiner, Z. B. Wang, and Z. H. Lu, Pitfalls in measuring work function using photoelectron spectroscopy, Appl. Surf. Sci. **256**, 2602 (2010).

[22] J. S. Kim, B. Lägel, E. Moons, N. Johansson, I. D. Baikie, W. R. Salaneck, R. H. Friend, and F. Cacialli, Kelvin probe and ultraviolet photoemission measurements of indium tin oxide work function: A comparison, Synth. Met. **111**, 311 (2000).

[23] M. M. Beerbom, B. Lägel, A. J. Cascio, B. V. Doran, and R. Schlaf, Direct comparison of photoemission spectroscopy and in situ Kelvin probe work function measurements on indium tin oxide films, J. Electron Spectrosc. Relat. Phenom. **152**, 12 (2006).

[24] O. W. Richardson, The emission of electricity from hot bodies, J. Röntgen Soc. **18**, 150 (1922).

[25] T. Schultz, P. Amsalem, N. B. Kotadiya, T. Lenz, P. W. M. Blom, and N. Koch, Importance of substrate work function homogeneity for reliable ionization energy determination by photoelectron spectroscopy, Phys. Status Solidi Basic Res. **256**, 1 (2019).

[26] M. J. Morant and H. House, The work function and patch field of an irregular metal surface, Proc. Phys. Soc., London, Sect. B **69**, 14 (1956).

[27] M. Xue, S. Peng, F. Wang, J. Ou, C. Li, and W. Li, Linear relation between surface roughness and work function of light alloys, J. Alloys Compd. **692**, 903 (2017).

[28] Y. Wan, Y. Li, Q. Wang, K. Zhang, and Y. Wu, The relationship of surface roughness and work function of pure silver by numerical modeling, Int. J. Electrochem. Sci. **7**, 5204 (2012).

[29] W. Li and D. Y. Li, On the correlation between surface roughness and work function in copper, J. Chem. Phys. **122**, 064708 (2005).

[30] J. Kaur and R. Kant, Theory of work function and potential of zero charge for metal nanostructured and rough electrodes, J. Phys. Chem. C **121**, 13059 (2017).

[31] N. Nakagiri and H. Kaizuka, Simulations of STM images and work function for rough surfaces, Jpn. J. Appl. Phys. **29**, 744 (1990).

[32] Z. Knor, Resolution of work function patches on atomically rough surfaces, Surf. Sci. **169**, 317 (1986).

[33] K. L. Jensen, M. McDonald, O. Chubenko, J. R. Harris, D. A. Shiffler, N. A. Moody, J. J. Petillo, and A. J. Jensen, Thermal-field and photoemission from meso- and micro-scale features: effects of screening and roughness on characterization and simulation, J. Appl. Phys. **125**, 234303 (2019).

[34] G. I. Kuznetsov and E. A. Sokolovsky, Dependence of effective work function for LaB_6 on surface conditions, Phys. Scr. **1997**, 130 (1997).

[35] W. Y. Li, K. Goto, and R. Shimizu, PEEM is a suitable tool for absolute work function measurements, Surf. Interface Anal. **37**, 244 (2005).

[36] D. Vogel, C. Spiel, Y. Suchorski, A. Urich, R. Schlögl, and G. Rupprechter, Mapping the local reaction kinetics by PEEM: CO oxidation on individual (100)-type grains of Pt foil, Surf. Sci. **605**, 1999 (2011).

[37] W. Engel, M. E. Kordesch, H. H. Rotermund, S. Kubala, and A. von Oertzen, A UHV-compatible photoelectron emission microscope for applications in surface science, Ultramicroscopy **36**, 148 (1991).

[38] C. Wang and M. E. Kordesch, The morphology of carbon films and surfaces studied by photoemission electron microscopy, Ultramicroscopy **36**, 154 (1991).

[39] K. Wandelt, The local work function: Concept and implications, Appl. Surf. Sci. **111**, 1 (1997).

[40] K. L. Jensen, *Electron Emission Physics* (Elsevier, San Diego, CA, USA, 2007), Vol. 149.

[41] P. O. Gartland, S. Berge, and B. J. Slagsvold, Photoelectric Work Function of a Copper Single Crystal for the (100), (110), (111), and (112) Faces, Phys. Rev. Lett. **28**, 738 (1972).

[42] F. Morini, E. Dubois, J. F. Robillard, S. Monfray, and T. Skotnicki, Low work function thin film growth for high efficiency thermionic energy converter: coupled Kelvin probe and photoemission study of potassium oxide, Phys. Status Solidi Appl. Mater. Sci. **211**, 1334 (2014).

[43] U. Zerweck, C. Loppacher, T. Otto, S. Grafström, and L. M. Eng, Accuracy and resolution limits of Kelvin probe force microscopy, Phys. Rev. B: Condens. Matter Mater. Phys. **71**, 1 (2005).

[44] M. Nonnenmacher, M. P. O'Boyle, and H. K. Wickramasinghe, Kelvin probe force microscopy, Appl. Phys. Lett. **58**, 2921 (1998).

[45] W. Melitz, J. Shen, A. C. Kummel, and S. Lee, Kelvin probe force microscopy and its application, Surf. Sci. Rep. **66**, 1 (2011).

[46] V. Palermo, M. Palma, and P. Samorì, Electronic characterization of organic thin films by Kelvin probe force microscopy, Adv. Mater. **18**, 145 (2006).

[47] S. Dushman, Thermionic emission, Rev. Mod. Phys. **2**, 381 (1930).

[48] C. Davisson and L. H. Germer, The thermionic work function of tungsten, Phys. Rev. **20**, 300 (1922).

[49] C. Davisson and L. H. Germer, A note on the thermionic work function of tungsten, Phys. Rev. **30**, 634 (1927).

[50] V. S. Fomenko, *Handbook of Thermionic Properties* (Springer US, Boston, MA, 1966).

[51] J. Voss, A. Vojvodic, S. H. Chou, R. T. Howe, I. Bargatin, and F. Abild-Pedersen, Thermionic current densities from first principles, J. Chem. Phys. **138**, 204701 (2013).

[52] H. Shelton, Thermionic emission from a planar tantalum crystal, Phys. Rev. **107**, 1553 (1957).

[53] F. A. M. Koeck, R. J. Nemanich, A. Lazea, and K. Haenen, Thermionic electron emission from low work-function phosphorus doped diamond films, Diam. Relat. Mater. **18**, 789 (2009).

[54] C. Herring and M. H. Nichols, Thermionic emission, Rev. Mod. Phys. **21**, 185 (1949).

[55] Y. S. Ang and L. K. Ang, Current-Temperature Scaling for a Schottky Interface with Nonparabolic Energy Dispersion, Phys. Rev. Appl. **6**, 034013 (2016).

[56] Y. S. Ang, H. Y. Yang, and L. K. Ang, Universal Scaling Laws in Schottky Heterostructures Based on Two-Dimensional Materials, Phys. Rev. Lett. **121**, 56802 (2018).

[57] Y. S. Ang, L. Cao, and L. K. Ang, Physics of electron emission and injection in two-dimensional materials: Theory and simulation, InfoMat **3**, 502 (2021).

[58] D. Chen, *Modeling Nonuniform Thermionic Emission from Heterogeneous Cathodes* (University of Wisconsin-Madison, Madison, WI, USA, 2022).

[59] S.-Y. Ning, T. Iitaka, X.-Y. Yang, Y. Wang, J.-J. Zhao, Z. Li, and J.-X. Zhang, Enhanced thermionic emission performance of LaB_6 by Ce doping, J. Alloys Compd. **760**, 1 (2018).

[60] E. B. Hensley, Thermionic emission constants and their interpretation, J. Appl. Phys. **32**, 301 (1961).

[61] R. A. Tuck, Surface studies of thermionic emitters by methods unique to them, Appl. Surf. Sci. **2**, 128 (1979).

[62] M. E. Kordesch, J. M. Vaughn, C. Wan, and K. D. Jamison, Model scandate cathodes investigated by thermionic-emission microscopy, J. Vac. Sci. Technol., B **29**, 4 (2011).

[63] R. H. Fowler and L. Nordheim, Electron emission in intense electric fields, Proc. R. Soc. London, Ser. A **119**, 173 (1928).

[64] X. Lu, Q. Yang, W. Chen, C. Xiao, and A. Hirose, Field electron emission characteristics of diamond films with different grain morphologies, J. Vac. Sci. Technol., B: Microelectron. Nanometer Struct.–Process., Meas., Phenom. **24**, 2575 (2006).

[65] R. G. Forbes, Refining the application of Fowler-Nordheim theory, Ultramicroscopy **79**, 11 (1999).

[66] R. G. Forbes, J. H. B. Deane, A. Fischer, and M. S. Mousa, Fowler-Nordheim plot analysis: A progress report, Jordan J. Phys. **8**, 125 (2015)

[67] M.-C. Lin and Y.-H. Liao, Fitting nonlinear Fowler-Nordheim plots of field emission strips with a self-consistent parallel plane model, J. Vac. Sci. Technol., B: Microelectron. Nanometer Struct.–Process., Meas., Phenom. **26**, 826 (2008).

[68] D. A. Shiffler, W. Tang, K. L. Jensen, K. Golby, M. LaCour, J. J. Petillo, and J. R. Harris, Effective field enhancement factor and the influence of emitted space charge, J. Appl. Phys. **118**, 083302 (2015).

[69] J. Jobst, L. M. Boers, C. Yin, J. Aarts, R. M. Tromp, and S. J. van der Molen, Quantifying work function differences using low-energy electron microscopy: The case of mixed-terminated strontium titanate, Ultramicroscopy **200**, 43 (2019).

[70] A. L. F. Cauduro, R. dos Reis, G. Chen, A. K. Schmid, H. G. Rubahn, and M. Madsen, Work function mapping of MoOx thin-films for application in electronic devices, Ultramicroscopy **183**, 1339 (2017).

[71] E. Wigner and J. Bardeen, Theory of the work functions of monovalent metals, Phys. Rev. **48**, 84 (1935).

[72] J. Bardeen, Theory of the work function. II. The surface double layer, Phys. Rev. **49**, 653 (1936).

[73] V. Russier and J. P. Badiali, Calculation of the electronic work function of Cu and Ag from an extended jellium model, Phys. Rev. B **39**, 13193 (1989).

[74] P. Hohenberg and W. Kohn, Inhomogeneous electron gas, Phys. Rev. **136**, B864 (1964).

[75] L. Bai, Y. Qie, T. Li, C. Zhang, S. Yang, Q. Li, and Q. Sun, Enhancing electron emission of Hf with an ultralow work function by barium-oxygen coatings, J. Phys. Chem. C **126**, 2806 (2022).

[76] R. Tran, X.-G. Li, J. H. Montoya, D. Winston, K. A. Persson, and S. P. Ong, Anisotropic work function of elemental crystals, Surf. Sci. **687**, 48 (2019).

[77] Q. Zhou, X. Liu, T. Maxwell, B. Vancil, T. J. Balk, and M. J. Beck, $Ba_xSc_yO_z$ on W (0 0 1), (1 1 0), and (1 1 2) in scandate cathodes: Connecting to experiment via μ O and equilibrium crystal shape, Appl. Surf. Sci. **458**, 827 (2018).

[78] V. Vlahos, J. H. Booske, and D. Morgan, Ab initio investigation of barium-scandium-oxygen coatings on tungsten for electron emitting cathodes, Phys. Rev. B **81**, 054207 (2010).

[79] C. J. Fall, N. Binggeli, and A. Baldereschi, Deriving accurate work functions from thin-slab calculations, J. Phys. Condens. Matter **11**, 2689 (1999).

[80] Y. L. Lee and D. Morgan, Ab initio defect energetics of perovskite (001) surfaces for solid oxide fuel cells: A comparative study of $LaMnO_3$ versus $SrTiO_3$ and $LaAlO_3$, Phys. Rev. B: Condens. Matter Mater. Phys. **91**, 195430 (2015).

[81] S. De Waele, K. Lejaeghere, M. Sluydts, and S. Cottenier, Error estimates for density-functional theory predictions of surface energy and work function, Phys. Rev. B **94**, 235418 (2016).

[82] M. Uijttewaal, G. De Wijs, and R. De Groot, Ab initio and work function and surface energy anisotropy of LaB_6, J. Phys. Chem. B **110**, 18459 (2006).

[83] K. M. Schmidt, S. T. Misture, O. A. Graeve, and V. R. Vasquez, Metal hexaboride work functions: Surface configurations and the electrical double layer from first-principles, Adv. Electron. Mater **5**, 1800074 (2019).

[84] M. G. Quesne, A. Roldan, N. H. De Leeuw, and C. R. A. Catlow, Bulk and surface properties of metal carbides: Implications for catalysis, Phys. Chem. Chem. Phys. **20**, 6905 (2018).

[85] Z. Zhong and P. Hansmann, Tuning the work function in transition metal oxides and their heterostructures, Phys. Rev. B **93**, 235116 (2016).

[86] S. A. Chambers and P. V. Sushko, Influence of crystalline order and defects on the absolute work functions and electron affinities of TiO_2- and SrO-terminated n-$SrTiO_3$(001), Phys. Rev. Mater. **3**, 125803 (2019).

[87] Y. Murata, E. Starodub, B. B. Kappes, C. V. Ciobanu, N. C. Bartelt, K. F. McCarty, and S. Kodambaka, Orientation-dependent work function of graphene on Pd(111), Appl. Phys. Lett. **97**, 143114 (2010).

[88] B. Wang, S. Günther, J. Wintterlin, and M. L. Bocquet, Periodicity, work function and reactivity of graphene on Ru(0001) from first principles, New J. Phys. **12**, 43041 (2010).

[89] G. Giovannetti, P. A. Khomyakov, G. Brocks, V. M. Karpan, J. Van Den Brink, and P. J. Kelly, Doping Graphene with Metal Contacts, Phys. Rev. Lett. **101**, 026803 (2008).

[90] H. A. Tahini, X. Tan, and S. C. Smith, The origin of low workfunctions in OH terminated MXenes, Nanoscale **9**, 7016 (2017).

[91] H. B. Michaelson, The work function of the elements and its periodicity, J. Appl. Phys. **48**, 4729 (1977).

[92] R. Jacobs, D. Morgan, and J. Booske, Work function and surface stability of tungsten-based thermionic electron emission cathodes work function and surface stability of tungsten-based thermionic electron emission cathodes, APL Mater. **5**, 116105 (2017).

[93] P. M. Zagwijn, J. W. M. Frenken, U. Van Slooten, and P. A. Duine, A model system for scandate cathodes, Appl. Surf. Sci. **111**, 35 (1997).

[94] T. Ma, R. Jacobs, J. Booske, and D. Morgan, Work function trends and new low-work-function boride and nitride materials for electron emission applications, J. Phys. Chem. C **125**, 17400 (2021).

[95] N. Erdman, O. Warschkow, M. Asta, K. R. Poeppelmeier, D. E. Ellis, and L. D. Marks, Surface structures of $SrTiO_3$(001): A TiO_2-rich reconstruction with a c(4 × 2) unit cell, J. Am. Chem. Soc. **125**, 10050 (2003).

[96] N. Erdman, K. R. Poeppelmeier, M. Asta, O. Warschkow, D. E. Ellis, and L. D. Marks, The structure and chemistry of the TiO_2-rich surface of $SrTiO_3$(001), Nature **419**, 55 (2002).

[97] Y. Lin, A. E. Becerra-Toledo, F. Silly, K. R. Poeppelmeier, M. R. Castell, and L. D. Marks, The (2 × 2) reconstructions on the $SrTiO_3$(001) surface: A combined scanning tunneling microscopy and density functional theory study, Surf. Sci. **605**, L51 (2011).

[98] J. M. P. Martirez, E. H. Morales, W. A. Saidi, D. A. Bonnell, and A. M. Rappe, Atomic and Electronic Structure of the $BaTiO_3$(001) $(\sqrt{5} \times \sqrt{5})R26.6°$ Surface Reconstruction, Phys. Rev. Lett. **109**, 256802 (2012).

[99] T. Kubo and H. Nozoye, Surface Structure of $SrTiO_3$, Phys. Rev. Lett. **86**, 1801 (2001).

[100] T. Ma, R. Jacobs, J. Booske, and D. Morgan, Discovery and engineering of low work function perovskite materials, J. Mater. Chem. C **9**, 12778 (2021).

[101] T. C. Leung, H. Hu, A. J. Liu, and M. C. Lin, Adsorbate induced modulation of strain effects on work functions of a tungsten (100) surface, Phys. Chem. Chem. Phys. **21**, 25763 (2019).

[102] C. Quarti, F. De Angelis, and D. Beljonne, Influence of surface termination on the energy level alignment at the $CH_3NH_3PbI_3$ perovskite/C60 interface, Chem. Mater. **29**, 958 (2017).

[103] K. A. Stoerzinger, R. Comes, S. R. Spurgeon, S. Thevuthasan, K. Ihm, E. J. Crumlin, and S. A. Chambers, Influence of $LaFeO_3$ surface termination on water reactivity, J. Phys. Chem. Lett. **8**, 1038 (2017).

[104] M. Chagas Da Silva, M. Lorke, B. Aradi, M. Farzalipour Tabriz, T. Frauenheim, A. Rubio, D. Rocca, and P. Deák, Self-Consistent Potential Correction for Charged Periodic Systems, Phys. Rev. Lett. **126**, 76401 (2021).

[105] N. Li, T. Zong, and Z. Zhang, in *2021 IEEE 6th International Conference on Big Data Analytics, ICBDA 2021* (Institute of Electrical and Electronics Engineers Inc., 2021), pp. 87–91.

[106] Y. Xiong, W. Chen, W. Guo, H. Wei, and I. Dabo, Data-driven analysis of the electronic-structure factors controlling the work functions of perovskite oxides, Phys. Chem. Chem. Phys. **23**, 6880 (2021).

[107] W. Hashimoto, Y. Tsuji, and K. Yoshizawa, Optimization of work function via bayesian machine learning combined with first-principles calculation, J. Phys. Chem. C **124**, 9958 (2020).

[108] P. Schindler, E. R. Antoniuk, G. Cheon, Y. Zhu, and E. J. Reed, Discovery of materials with extreme work functions by high-throughput density functional theory and machine learning, ArXiv (2020).

[109] S. Yamamoto, K. Susa, and U. Kawabe, Work functions of binary compounds, J. Chem. Phys. **60**, 4076 (1974).

[110] T. Xie and J. C. Grossman, Crystal Graph Convolutional Neural Networks for an Accurate and Interpretable Prediction of Material Properties, Phys. Rev. Lett. **120**, 145301 (2018).
[111] V. Fung, J. Zhang, E. Juarez, and B. G. Sumpter, Benchmarking graph neural networks for materials chemistry, Npj Comput. Mater. **7**, 1 (2021).
[112] D. M. Kirkwood, S. J. Gross, T. J. Balk, M. J. Beck, J. Booske, D. Busbaher, R. Jacobs, M. E. Kordesch, B. Mitsdarffer, D. Morgan, W. D. Palmer, B. Vancil, and J. E. Yater, Frontiers in thermionic cathode research, IEEE Trans. Electron Devices **65**, 2061 (2018).
[113] R. T. Tung, Recent advances in Schottky barrier concepts, Mater. Sci. Eng. R Rep. **35**, 1 (2001).
[114] J. Y. Cheon, J. H. Kim, J. H. Kim, K. C. Goddeti, J. Y. Park, and S. H. Joo, Intrinsic relationship between enhanced oxygen reduction reaction activity and nanoscale work function of doped carbons, J. Am. Chem. Soc. **136**, 8875 (2014).
[115] R. Rössler, C. Leendertz, L. Korte, N. Mingirulli, B. Rech, R. Rößler, C. Leendertz, L. Korte, N. Mingirulli, and B. Rech, Impact of the transparent conductive oxide work function on injection-dependent a-si:h/c-si band bending and solar cell parameters, J. Appl. Phys. **113**, 144513 (2013).
[116] S. Garbe, CsF, Cs as a low work function layer on the GaAs photocathode, Phys. Status Solidi A **2**, 497 (1970).
[117] S. Xia, L. Liu, Y. Diao, and Y. Kong, Cs and Cs/O adsorption mechanism on GaN nanowires photocathode, J. Mater. Sci. **52**, 5661 (2017).
[118] Z. Cui, E. Li, X. Ke, T. Zhao, Y. Yang, Y. Ding, T. Liu, Y. Qu, and S. Xu, Adsorption of alkali-metal atoms on GaN nanowires photocathode, Appl. Surf. Sci. **423**, 829 (2017).
[119] W. He, S. Vilayurganapathy, A. G. Joly, T. C. Droubay, S. A. Chambers, J. R. Maldonado, and W. P. Hess, Comparison of CsBr and KBr covered Cu photocathodes: Effects of laser irradiation and work function changes, Appl. Phys. Lett. **102**, 071604 (2013).
[120] H. Zhang, J. Tang, J. Yuan, J. Ma, N. Shinya, K. Nakajima, H. Murakami, T. Ohkubo, and L. C. Qin, Nanostructured LaB_6 field emitter with lowest apical work function, Nano Lett. **10**, 3539 (2010).
[121] M. Nakamoto, T. Hasegawa, T. Ono, T. Sakai, and N. Sakuma, in *Technical Digest - International Electron Devices Meeting, IEDM* (1996), pp. 297–300.
[122] M. Nakamoto and J. Moon, Suitability of low-work-function titanium nitride coated transfer mold field-emitter arrays for harsh environment applications, J. Vac. Sci. Technol., B: Microelectron. Nanometer Struct.–Process., Meas., Phenom. **29**, 02B112 (2011).
[123] R. U. Martinelli and D. G. Fisher, The application of semiconductors with negative electron affinity surfaces to electron emission devices, Proc. IEEE **62**, 1339 (1974).
[124] J. Van Der Weide, Z. Zhang, P. K. Baumann, M. G. Wensell, J. Bernholc, and R. J. Nemanich, Negative-electron-affinity effects on the diamond (100) surface, Phys. Rev. B **50**, 5803 (1994).
[125] R. J. Nemanich, P. K. Baumann, M. C. Benjamin, S. W. King, J. Van Der Weide, and R. F. Davis, negative electron affinity surfaces of aluminum nitride and diamond, Diam. Relat. Mater. **5**, 790 (1996).
[126] I. V. Bazarov, B. M. Dunham, Y. Li, X. Liu, D. G. Ouzounov, C. K. Sinclair, F. Hannon, and T. Miyajima, Thermal emittance and response time measurements of negative electron affinity photocathodes, J. Appl. Phys. **103**, 054901 (2008).
[127] H. Yamaguchi, T. Masuzawa, S. Nozue, Y. Kudo, I. Saito, J. Koe, M. Kudo, T. Yamada, Y. Takakuwa, and K. Okano, Electron emission from conduction band of diamond with negative electron affinity, Phys. Rev. B: Condens. Matter Mater. Phys. **80**, 165321 (2009).
[128] F. Rezaeifar, H. U. Chae, R. Ahsan, and R. Kapadia, Hot electron emission from waveguide integrated lanthanum hexaboride nanoparticles, Appl. Phys. Lett. **118**, 071108 (2021).
[129] F. Rezaeifar, R. Ahsan, Q. Lin, H. U. Chae, and R. Kapadia, Hot-electron emission processes in waveguide-integrated graphene, Nat. Photonics **13**, 843 (2019).
[130] G. Gaertner and D. Den Engelsen, Hundred years anniversary of the oxide cathode - a historical review, Appl. Surf. Sci. **251**, 24 (2005).
[131] G. A. Haas, Analysis of the dc and pulsed thermionic emission from BaO, J. Appl. Phys. **28**, 1486 (1957).
[132] L. E. Grey, Thermionic emission from the BaO-CaO system, Nature **165**, 773 (1950).
[133] M. Futamoto, M. Nakazawa, K. Usami, S. Hosoki, and U. Kawabe, Thermionic emission properties of a single-crystal LaB_6 cathode, J. Appl. Phys. **51**, 3869 (1980).
[134] M. Futamoto, M. Nakazawa, and U. Kawabe, Thermionic emission properties of hexaborides, Surf. Sci. **100**, 470 (1980).
[135] G. H. Olsen and A. V. Cafiero, Single-crystal growth of mixed (La, Eu, Y, Ce, Ba, Cs) hexaborides for thermionic emission, J. Cryst. Growth **44**, 287 (1978).
[136] J.-M. Roquais, B. Vancil, and M. Green, in *Modern Developments in Vacuum Electron Sources*, edited by G. Gaertner, W. Knapp, R. G. Forbes (Springer International Publishing, Cham, 2020), pp. 33–82.
[137] J. A. J. M. Deckers, T. H. Weekers, A. Manenschijn, F. M. M. Snijkers, and P. A. M. Van Der Heide, Dispenser cathode and method of manufacturing a dispenser cathode, 5,666,022 (1997).
[138] R. Garg, N. Dutta, and N. Choudhury, Work function engineering of graphene, Nanomaterials **4**, 267 (2014).
[139] S. Halas and T. Durakiewicz, Physical foundations of the oxide cathodes, Appl. Surf. Sci. **252**, 6119 (2006).
[140] M. P. Kirley, B. Novakovic, N. Sule, M. J. Weber, I. Knezevic, and J. H. Booske, Effect of sputtered lanthanum hexaboride film thickness on field emission from metallic knife edge cathodes, J. Appl. Phys. **111**, 063717 (2012).
[141] H. Yamauchi, K. Takagi, I. Yuito, and U. Kawabe, Work function of LaB_6, Appl. Phys. Lett. **29**, 638 (1976).
[142] R. Jenkins, A review of thermionic cathodes, Vacuum **19**, 353 (1969).
[143] M. N. Seif, Q. Zhou, X. Liu, T. J. Balk, and M. J. Beck, Sc-containing (scandate) thermionic cathodes: Fabrication, microstructure, and emission performance, IEEE Trans. Electron Devices **69**, 3513 (2022).

[144] M. N. Seif, Q. Zhou, X. Liu, T. J. Balk, and M. J. Beck, Sc-containing (scandate) thermionic cathodes: Mechanisms for Sc enhancement of emission, IEEE Trans. Electron Devices **69**, 3523 (2022).

[145] L. Lin, R. Jacobs, D. Chen, V. Vlahos, O. Lu-Steffes, J. A. Alonso, D. Morgan, and J. Booske, Demonstration of low work function perovskite $SrVO_3$ using thermionic electron emission, Adv. Funct. Mater. **32**, 2203703 (2022).

[146] S. M. Sze and K. K. Ng, *Physics of Semiconductor Devices* (John Wiley & Sons, Hoboken, New Jersey, USA, 2006).

[147] J. Tersoff, Schottky Barrier Heights and the Continuum of Gap States, Phys. Rev. Lett. **52**, 465 (1984).

[148] G. Çankaya and N. Uçar, Schottky barrier height dependence on the metal work function for p-type Si Schottky diodes, Z. Naturforsch., A **59**, 795 (2004).

[149] M. Minohara, R. Yasuhara, H. Kumigashira, and M. Oshima, Termination layer dependence of Schottky barrier height for $La_{0.6}Sr_{0.4}MnO_3/Nb:SrTiO_3$ heterojunctions, Phys. Rev. B: Condens. Matter Mater. Phys. **81**, 235322 (2010).

[150] J. L. Freeouf and J. M. Woodall, Schottky barriers: An effective work function model, Appl. Phys. Lett. **39**, 727 (1981).

[151] A. C. Schmilz, A. T. Ping, M. Asif Khan, Q. Chen, J. W. Yang, and I. Adesida, Schottky barrier properties of various metals on n-type GaN, Semicond. Sci. Technol. **11**, 1464 (1996).

[152] Y. Zhou, *et al.*, A universal method to produce low-work function electrodes for organic electronics, Science **336**, 327 (2012).

[153] S. Heinze, J. Tersoff, R. Martel, V. Derycke, J. Appenzeller, and P. Avouris, Carbon Nanotubes as Schottky Barrier Transistors, Phys. Rev. Lett. **89**, 106801 (2002).

[154] K. Piskorski and H. M. Przewlocki, in *MIPRO 2010 - 33rd International Convention on Information and Communication Technology, Electronics and Microelectronics, Proceedings* (2010), pp. 37–42.

[155] B. Y. Tsui and C. F. Huang, Wide range work function modulation of binary alloys for MOSFET application, IEEE Electron Device Lett. **24**, 153 (2003).

[156] A. Bhalla and S. K. Lui, MOSFET using gate work function engineering for switching applications, *US 8,119,482 B2* (23 December 2012).

[157] S. Deb, N. B. Singh, N. Islam, and S. K. Sarkar, Work function engineering with linearly graded binary metal alloy gate electrode for short-channel SOI MOSFET, IEEE Trans. Nanotechnol. **11**, 472 (2012).

[158] Y. T. Hou, M. F. Li, T. Low, and D. L. Kwong, Metal gate work function engineering on gate leakage of MOSFETs, IEEE Trans. Electron Devices **51**, 1783 (2004).

[159] Y. Lee and C. Shin, Impact of equivalent oxide thickness on threshold voltage variation induced by work-function variation in multigate devices, IEEE Trans. Electron Devices **64**, 2452 (2017).

[160] H. Nam and C. Shin, Impact of current flow shape in tapered (versus rectangular) finFET on threshold voltage variation induced by work-function variation, IEEE Trans. Electron Devices **61**, 2007 (2014).

[161] Y. K. Choi, L. Chang, P. Ranade, J. S. Lee, D. Ha, S. Balasubramanian, A. Agarwal, M. Ameen, T. J. King, and J. Bokor, in *Technical Digest - International Electron Devices Meeting* (2002), pp. 259–262.

[162] R. Ma, G. Lin, Y. Zhou, Q. Liu, T. Zhang, G. Shan, M. Yang, and J. Wang, A review of oxygen reduction mechanisms for metal-free carbon-based electrocatalysts, Npj Comput. Mater. **5**, 1 (2019).

[163] C. G. Vayenas, S. Bebelis, and S. Ladas, Dependence of catalytic rates on catalyst work function, Nature **343**, 625 (1990).

[164] C. G. Vayenas, S. Bebelis, C. Pliangos, S. Brosda, and D. Tsiplakides, *Electrochemical Activation of Catalysis: Promotion, Electrochemical Promotion, and Metal-Support Interactions* (Springer, New York, USA, 2001).

[165] K. A. Stoerzinger, M. Risch, J. Suntivich, W. M. Lü, J. Zhou, M. D. Biegalski, H. M. Christen, Ariando, T. Venkatesan, and S. H. Yang, Oxygen electrocatalysis on (001)-oriented manganese perovskite films: Mn valency and charge transfer at the nanoscale, Energy Environ. Sci. **6**, 1582 (2013).

[166] W. T. Hong, K. A. Stoerzinger, B. Moritz, T. P. Devereaux, W. Yang, and Y. Shao-Horn, Probing $LaMO_3$ metal and oxygen partial density of states using x-ray emission, absorption, and photoelectron spectroscopy, J. Phys. Chem. C **119**, 2063 (2015).

[167] S. Trasatti, Structure of the metal/electrolyte solution interface: New data for theory, Electrochim. Acta **36**, 1659 (1991).

[168] F. Calle-Vallejo, M. T. M. Koper, and A. S. Bandarenka, Tailoring the catalytic activity of electrodes with monolayer amounts of foreign metals, Chem. Soc. Rev. **42**, 5210 (2013).

[169] B. Łosiewicz, M. Popczyk, I. Napłoszek, and A. Budniok, Intermetallic compounds as catalysts in the reaction of electroevolution/absorption of hydrogen, Solid State Phenom. **228**, 16 (2015).

[170] G. Kumar, S. L. J. Lau, M. D. Krcha, and M. J. Janik, Correlation of methane activation and oxide catalyst reducibility and its implications for oxidative coupling, ACS Catal. **6**, 1812 (2016).

[171] R. Jacobs, J. Hwang, Y. Shao-Horn, and D. Morgan, Assessing correlations of perovskite catalytic performance with electronic structure descriptors, Chem. Mater. **31**, 785 (2019).

[172] R. Jacobs, T. Mayeshiba, J. Booske, and D. Morgan, Material discovery and design principles for stable, high activity perovskite cathodes for solid oxide fuel cells, Adv. Energy Mater. **8**, 1702708 (2018).

[173] L. Giordano, K. Akkiraju, R. Jacobs, D. Vivona, D. Morgan, and Y. Shao-Horn, Electronic structure-based descriptors for oxide properties and functions, Acc. Chem. Res. **55**, 298 (2022).

[174] A. Grimaud, K. J. May, C. E. Carlton, Y. L. Lee, M. Risch, W. T. Hong, J. Zhou, and Y. Shao-Horn, Double Perovskites as a family of highly active catalysts for oxygen evolution in alkaline solution, Nat. Commun. **4**, 1 (2013).

[175] D. Lee, Y. L. Lee, W. T. Hong, M. D. Biegalski, D. Morgan, and Y. Shao-Horn, Oxygen surface exchange kinetics and stability of $(La,Sr)_2CoO_{4\pm\delta}/La_{1-X}Sr_XMO_{3-\delta}$

(M = Co and Fe) hetero-interfaces at intermediate temperatures, J. Mater. Chem. A **3**, 2144 (2015).
[176] L. Tang, X. Meng, D. Deng, and X. Bao, Confinement catalysis with 2D materials for energy conversion, Adv. Mater. **31**, 1 (2019).
[177] G. Hua and D. Li, Generic relation between the electron work function and Young's modulus of metals, Appl. Phys. Lett. **99**, 41907 (2011).
[178] R. Rahemi and D. Li, Variation in electron work function with temperature and its effect on the Young's modulus of metals, Scr. Mater. **99**, 41 (2015).
[179] G. Hua and D. Li, The correlation between the electron work function and yield strength of metals, Phys. Status Solidi B Basic Res. **249**, 1517 (2012).
[180] H. Lu and D. Li, Correlation between the electron work function of metals and their bulk moduli, thermal expansion and heat capacity via the Lennard-Jones potential, Phys. Status Solidi B Basic Res. **251**, 815 (2014).
[181] H. Lu, Z. Liu, X. Yan, D. Li, L. Parent, and H. Tian, Electron Work Function-a Promising Guiding Parameter for Material Design, Sci. Rep. **6**, 1 (2016).
[182] D. Y. Li, L. Guo, L. Li, and H. Lu, Electron work function - a probe for interfacial diagnosis, Sci. Rep. **7**, 1 (2017).
[183] K. A. A. Khalid, T. J. Leong, and K. Mohamed, Review on thermionic energy converters, IEEE Trans. Electron Devices **63**, 2231 (2016).
[184] B. Qi and J. Wang, Open-circuit voltage in organic solar cells, J. Mater. Chem. **22**, 24315 (2012).
[185] E. Centurioni and D. Iencinella, Role of front contact work function on amorphous silicon/crystalline silicon heterojunction solar cell performance, IEEE Electron Device Lett. **24**, 177 (2003).
[186] E. Fortunato, D. Ginley, H. Hosono, and D. C. Paine, Transparent conducting oxides for photovoltaics, MRS Bull. **32**, 242 (2007).
[187] A. Klein, C. Körber, A. Wachau, F. Säuberlich, Y. Gassenbauer, S. P. Harvey, D. E. Proffit, and T. O. Mason, Transparent conducting oxides for photovoltaics: manipulation of fermi level, work function and energy band alignment, Materials (Basel) **3**, 4892 (2010).
[188] P. H. Lee, T. T. Wu, K. Y. Tian, C. F. Li, C. H. Hou, J. J. Shyue, C. F. Lu, Y. C. Huang, and W. F. Su, Work-function-tunable electron transport layer of molecule-capped metal oxide for a high-efficiency and stable p-i-n perovskite solar cell, ACS Appl. Mater. Interfaces **12**, 45936 (2020).
[189] M. F. Mohamad Noh, C. H. Teh, R. Daik, E. L. Lim, C. C. Yap, M. A. Ibrahim, N. Ahmad Ludin, A. R. Bin Mohd Yusoff, J. Jang, and M. A. Mat Teridi, The architecture of the electron transport layer for a perovskite solar cell, J. Mater. Chem. C **6**, 682 (2018).
[190] A. Varpula, S. J. Laakso, T. Havia, J. Kyynäräinen, and M. Prunnila, Harvesting vibrational energy using material work functions, Sci. Rep. **4**, 1 (2014).
[191] C. Beasley, M. Kumaran Gnanamani, E. Santillan-Jimenez, M. Martinelli, W. D. Shafer, S. D. Hopps, N. Wanninayake, and D. Y. Kim, Effect of metal work function on hydrogen production from photocatalytic water splitting with $MTiO_2$ catalysts, ChemistrySelect **5**, 1013 (2020).
[192] K. H. Ye, H. Li, D. Huang, S. Xiao, W. Qiu, M. Li, Y. Hu, W. Mai, H. Ji, and S. Yang, Enhancing photoelectrochemical water splitting by combining work function tuning and heterojunction engineering, Nat. Commun. **10**, 1 (2019).
[193] Y. Gao, Z. Wang, and L. Chen, Workfunction, a new viewpoint to understand the electrolyte/electrode interface reaction, J. Mater. Chem. A **3**, 23420 (2015).
[194] R. E. Warburton, J. J. Kim, S. Patel, J. D. Howard, L. A. Curtiss, C. Wolverton, D. B. Buchholz, J. T. Vaughey, P. Fenter, T. T. Fister, and J. Greeley, Tailoring interfaces in solid-state batteries using interfacial thermochemistry and band alignment, Chem. Mater. **33**, 8447 (2021).
[195] F. Li, X. Gao, R. Wang, T. Zhang, and G. Lu, Study on TiO_2-SnO_2 core-shell heterostructure nanofibers with different work function and its application in gas sensor, Sens. Actuators B Chem. **248**, 812 (2017).
[196] K. C. Kwon, K. S. Choi, and S. Y. Kim, Increased work function in few-layer graphene sheets via metal chloride doping, Adv. Funct. Mater. **22**, 4724 (2012).
[197] F. Gossenberger, T. Roman, K. Forster-Tonigold, and A. Groß, Change of the work function of platinum electrodes induced by halide adsorption, Beilstein J. Nanotechnol. **5**, 152 (2014).
[198] M. T. Greiner, L. Chai, M. G. Helander, W. M. Tang, and Z. H. Lu, Transition metal oxide work functions: The influence of cation oxidation state and oxygen vacancies, Adv. Funct. Mater. **22**, 4557 (2012).
[199] X. Peng, F. Tang, and A. Copple, Engineering the work function of armchair graphene nanoribbons using strain and functional species: A first principles study, J. Phys. Condens. Matter. **24**, 075501 (2012).
[200] F. J. Himpsel, J. A. Knapp, J. A. Vanvechten, and D. E. Eastman, Quantum photoyield of diamond(111) a stable negative-affinity emitter, Phys. Rev. B **20**, 624 (1979).
[201] V. Vlahos, Y. L. Lee, J. H. Booske, D. Morgan, L. Turek, M. Kirshner, R. Kowalczyk, and C. Wilsen, Ab initio investigation of the surface properties of dispenser B-type and scandate thermionic emission cathodes, Appl. Phys. Lett. **94**, 2007 (2009).
[202] G. N. Derry and P. N. Ross, A work function change study of oxygen adsorption on Pt(111) and Pt(100), J. Chem. Phys. **82**, 2772 (1998).
[203] T. Schultz, J. Niederhausen, and R. Schlesinger, Impact of surface states and bulk doping level on hybrid inorganic/organic semiconductor interface energy levels, J. Appl. Phys. **123**, 245501 (2018).
[204] T. C. Cheng, J. Shieh, W. J. Huang, M. C. Yang, M. H. Cheng, H. M. Lin, and M. N. Chang, Hydrogen plasma dry etching method for field emission application, Appl. Phys. Lett. **88**, 263118 (2006).
[205] H. L. Skriver and N. M. Rosengaard, Surface energy and work function of elemental metals, Phys. Rev. B **46**, 7157 (1992).
[206] J. J. Uebbing and L. W. James, Behavior of cesium oxide as a low work-function coating, J. Appl. Phys. **41**, 4505 (1970).
[207] K. Shen, R. Yang, D. Wang, M. Jeng, S. Chaudhary, K. Ho, and D. Wang, Stable CdTe solar cell with V_2O_5 as

a back contact buffer layer, Sol. Energy Mater. Sol. Cells **144**, 500 (2016).

[208] T. Susaki, A. Makishima, and H. Hosono, Work function engineering via $LaAlO_3/SrTiO_3$ polar interfaces, Phys. Rev. B: Condens. Matter Mater. Phys. **84**, 115456 (2011).

[209] F. Hess and B. Yildiz, Polar or not polar? The interplay between reconstruction, Sr enrichment, and reduction at the $La_{0.75}Sr_{0.25}MnO_3(001)$ surface, Phys. Rev. Mater. **4**, 15801 (2020).

[210] J. W. Harter, L. Maritato, D. E. Shai, E. J. Monkman, Y. Nie, D. G. Schlom, and K. M. Shen, Doping evolution and polar surface reconstruction of the infinite-layer cuprate $Sr_{1-X}La_XCuO_2$, Phys. Rev. B: Condens. Matter Mater. Phys. **92**, 035149 (2015).

[211] S. Hong, S. M. Nakhmanson, and D. D. Fong, Screening mechanisms at polar oxide heterointerfaces, Rep. Prog. Phys. **79**, 076501 (2016).

[212] K. C. L. Bauerfeind, R. Roß, and T. Bredow, Theoretical study of polar spinel surfaces: Effect of termination and cation inversion on structure and stability, J. Phys. Chem. C **124**, 28520 (2020).

[213] H. Yuan, S. Chang, I. Bargatin, N. C. Wang, D. C. Riley, H. Wang, J. W. Schwede, J. Provine, E. Pop, Z. X. Shen, P. A. Pianetta, N. A. Melosh, and R. T. Howe, Engineering ultra-low work function of graphene, Nano Lett. **15**, 6475 (2015).

[214] A. Di Vito, A. Pecchia, M. Auf der Maur, and A. Di Carlo, Nonlinear work function tuning of lead-halide perovskites by MXenes with mixed terminations, Adv. Funct. Mater. **1909028**, 1 (2020).

[215] C. Leung, L. Kao, S. Su, J. Feng, and T. Chan, Relationship between surface dipole, work function and charge transfer: some exceptions to an established rule, Phys. Rev. B: Condens. Matter Mater. Phys. **68**, 195408 (2003).

[216] P. R. Norton, J. W. Goodale, and E. B. Selkirk, Adsorption of Co on Pt(111) studied by photoemission, thermal desorption spectroscopy and high resolution dynamic measurements of work function, Surf. Sci. **83**, 189 (1979).

[217] G. S. Tompa, W. E. Carr, and M. Seidl, Work function reduction of a tungsten surface due to cesium ion bombardment, Appl. Phys. Lett. **49**, 1511 (1986).

[218] Y. H. Joo, M. J. Jin, S. K. Kim, D. S. Um, and C. Il Kim, BCl_3/Ar plasma etching for the performance enhancement of Al-doped ZnO thin films, Appl. Surf. Sci. **561**, 149957 (2021).

[219] M. Bruening, E. Moons, D. Cahen, and A. Shanzer, Controlling the work function of CdSe by chemisorption of benzoic acid derivatives and chemical etching, J. Phys. Chem. **99**, 8368 (1995).